Cryo-electron tomography of ASC signalling sites in pyroptotic cells

Yangci Liu[1,2], Haoming Zhai[1,2], Helen Alemayehu[1,2], Lee J. Hopkins[3,4], Alicia C. Borgeaud[5], Christina Heroven[5], Jonathan D. Howe[5], Jérôme Boulanger[5], Clare E. Bryant[3,4,*] & Yorgo Modis[1,2,*]

[1]Molecular Immunity Unit, Department of Medicine, University of Cambridge, MRC Laboratory of Molecular Biology, Francis Crick Avenue, Cambridge, CB2 0QH, United Kingdom

[2]Cambridge Institute of Therapeutic Immunology & Infectious Disease (CITIID), University of Cambridge School of Clinical Medicine, Cambridge CB2 0AW, United Kingdom

[3]Department of Medicine, University of Cambridge, Box 157, Level 5, Addenbrooke's Hospital, Cambridge, CB2 0QQ, United Kingdom

[4]Department of Veterinary Medicine, University of Cambridge, Madingley Road, Cambridge CB3 0ES, United Kingdom

[5]MRC Laboratory of Molecular Biology, Francis Crick Avenue, Cambridge, CB2 0QH, United Kingdom

Current addresses: Institute of Biochemistry and Molecular Medicine, University of Bern, Bühlstrasse 28, 3012 Bern, Switzerland (A.C.B.); Wren Therapeutics, Clarendon House, Clarendon Road, Cambridge CB2 8FH, UK (L.J.H.).

*Corresponding authors: C.E.B., ceb27@cam.ac.uk; Y.M., ymodis@mrc-lmb.cam.ac.uk

Abstract

Inflammasomes induce cell death in response to infection, chemical entities and cell damage. Human genetics and animal models have identified the NLRP3 inflammasome as a gatekeeper of caspase-1-dependent pyroptosis. NLRP3 activation induces polymerization of ASC into a single, micron-scale perinuclear punctum, where caspase-1 is activated. These puncta have yet to be imaged at sufficient resolution to resolve their ultrastructure. Here, we apply correlative cryo-light microscopy and cryo-electron tomography to visualize ASC/caspase-1 puncta and mitochondrial membrane remodelling within NLRP3-activated cells. The puncta are composed primarily of branched ASC filaments. The N-terminal pyrin domain forms an 8-10 nm-diameter tubular core, which is decorated by the flexibly linked C-terminal caspase recruitment domain. The variable filament density allows ribosomes and *trans*-Golgi-like vesicles to permeate the network. We propose this provides structural integrity while allowing macromolecules and vesicles to diffuse in or bind with the necessary density, timing and localization.

Keywords

NLR family pyrin domain containing 3 (NLRP3); apoptosis-associated speck-like protein containing a CARD (ASC) speck; caspase-1; pyroptosis; correlative light and electron microscopy (CLEM); *In situ* cryo-electron tomography (cryo-ET); focused-ion beam (FIB) milling; inflammasome; caspase activation and recruitment domain (CARD); pyrin domain (PYD)

Running title: Cryo-ET of ASC specks and mitochondria in cell lamellae

Introduction

Inflammasomes are vital innate immune oligomeric signalling complexes that induce proteolytic activation of caspase-1, leading to secretion of proinflammatory cytokines interleukin (IL)-1β and IL-18, and cell death by gasdermin D-driven pyroptosis. In the first step of inflammasome assembly, Nod-like receptors (NLR) sense cytosolic chemical signatures associated with microbes and cell dysfunction or damage[1]. Ligand binding induces NLR oligomerization and recruitment of downstream proteins linked to the caspase-1 signalling cascade.

NLRP3 is one of the most studied inflammasome NLRs due to the large number of NLRP3 genetic variants associated with human diseases and the availability of animal disease models. At least 250 human NLRP3 protein variants have been identified, over 30 of which have been associated with disease through gain-of-function[2,3], including autoinflammatory diseases, degenerative disorders, dermatitis and metabolic disorders[4,5]. NLRP3 inflammasome activation has been linked to a broad spectrum of cellular processes or cytosolic chemical signatures including potassium efflux, reactive oxygen species, calcium influx, chloride efflux, phosphatidylinositol-4-phosphate on Golgi membranes, and mitochondrial stress or damage[6,7]. Cryo-electron microscopy (cryo-EM) single-particle image reconstructions show that ligand-bound inflammasome NLRs assemble into disk- or split washer-like oligomers[8-11]. In addition to ligand recognition, activation of the NLRP3 and pyrin inflammasomes requires active transport along microtubules by dynein to the microtubule organizing centre (MTOC)[12,13]. Upon activation, NLRP3 recruits the adaptor protein ASC (Apoptosis-associated speck-like protein containing a caspase recruitment domain (CARD)). NLRP3 and ASC interact through their pyrin domains (PYDs)[14]. ASC then assembles into a single perinuclear punctum with a micron-scale diameter, also known as a speck, which functions as a platform for the recruitment and activation of caspase-1[15,16]. The PYD and CARD of ASC are both required for punctum formation and signalling[15,17,18]. Structural studies on purified ASC PYD and ASC CARD show that both

65 domains have a death fold and independently form helical filaments[19-24]. In the cell, fluorescence
66 microscopy imaging suggests that PYD-PYD interactions drive ASC filament formation whereas
67 CARD-CARD interactions promote cross-linking and compaction of PYD filaments into
68 puncta[17,18,23-26]. In addition, ASC recruits procaspase-1 via a CARD-CARD interaction between
69 the two proteins[15,23]. Super-resolution light microscopy of endogenous ASC specks revealed
70 punctate structures containing ASC, caspase 1 and NLRP3 within the same macro-assembly[27].
71 These structures have yet to be imaged inside a cell at sufficient resolution to resolve the ASC
72 or caspase-1 ultrastructure within puncta[26]. Hence, it remains unclear how the PYD and CARD
73 contribute to the formation of an ASC punctum inside cells.

74 Understanding how ASC filament formation contributes to the assembly and activation of
75 inflammasome puncta requires structural information in the cellular context. Recent advances in
76 the preparation of frozen vitrified cellular lamellae by focused ion-beam (FIB) milling[28,29] have
77 allowed the ultrastructure of multimeric protein complexes to be determined in a near-native
78 context by cryo-electron tomography (cryo-ET). Here, we use *in situ* cryo-ET to obtain three-
79 dimensional image reconstructions of multimeric signalling complexes in cells with active
80 NLRP3 inflammasomes. We identify ASC/caspase-1 signalosome puncta by correlative light
81 and electron microscopy (CLEM) and reveal their ultrastructure and pyroptotic cellular
82 landscape in immortalised bone marrow derived macrophages (iBMDMs) by cryo-ET image
83 reconstruction. We find that inflammasome puncta are composed of short, hollow ASC/caspase-
84 1 filaments, extensively branched, with variable packing density allowing ribosomes and certain
85 other cellular components to permeate the puncta. We propose that this ultrastructure of the
86 ASC filament network functions as a signalling platform by providing structural integrity while
87 allowing downstream signalling molecules to diffuse freely and bind at high density within the
88 network.

Results

In situ cryo-CLEM of ASC/caspase-1 puncta

High-resolution structures of inflammasome components have been obtained from purified proteins. In a previous study in zebrafish larvae, electron tomography of ASC puncta in fixed larval sections stained with uranyl acetate showed that the puncta contained a dense filament network[26], but the imaging resolution was limited by chemical fixation and staining of the sample. To examine the architecture and cellular interactions of the mammalian NLRP3 signalosome in its physiological environment, we imaged ASC puncta in iBMDMs by correlative fluorescence light microscopy and *in situ* cryo-ET (cryo-CLEM). Cells expressing ASC fused with a C-terminal fluorescent protein have been used extensively to visualize ASC puncta formation[30]. In some experimental systems, ASC overexpression can lead to puncta formation in the absence of activating inflammasome stimuli[30]. Fluorescence microscopy of live iBMDM cells overexpressing ASC-mCerulean used in this study showed that both priming with lipopolysaccharide (LPS) and stimulation with nigericin were still required to induce ASC puncta formation (**Fig. S1a, Movie S1**). Gasdermin D cleavage observed by Western blotting and IL-1β cytokine release measured in ELISAs confirmed that the ASC-mCerulean puncta activated pyroptotic signalling (**Fig. S1b**). Limiting the stimulation time with nigericin to 30 min allowed early-stage inflammasome signalling complexes to be captured, as indicated by colocalization of NLRP3, proteolytically activated caspase-1 and IL-1β with ASC in the puncta, in both wild-type (WT) iBMDMs and ASC-mCerulean iBMDMs (**Fig. S1c-e**). NLRP3 and IL-1β localization was determined by immunofluorescence. Caspase-1 localization was inferred using the carboxyfluorescein-labelled caspase-1 substrate FAM-FLICA. FAM-FLICA or its non-fluorescent analogue Z-VAD-FMK also facilitated imaging by delaying pyroptotic cell death (**Movies S1, S2**).

113 For high-resolution imaging, cells grown on electron microscopy grids were vitrified by
114 plunge-freezing in liquid ethane. We used both iBMDMs overexpressing ASC-mCerulean and
115 WT iBMDMs labelled with FAM-FLICA after NLRP3 inflammasome activation[31]. ASC/caspase-1
116 signalling complexes were located by cryo-fluorescence light microscopy (cryo-FM; **Fig. S2a**).
117 Areas of the frozen cells containing an ASC or caspase punctum were FIB-milled down to
118 lamellae 150-300 nm-thick and 15-20 µm wide[28,29], with micro-expansion joints to reduce
119 bending[32] (**Fig. S2b,c**). The lamellae were imaged by cryo-CLEM, using cryo-FM to locate any
120 remaining fluorescent signal from ASC-mCerulean or FAM-FLICA in the lamellae after milling
121 (**Fig. 1a,b; Fig. S2d,e**). The micron-scale dimensions of the fluorescent puncta allowed cryo-ET
122 tilt-series acquisition at regions of interest with the necessary targeting precision after
123 correlation of the cryo-FM images with low-magnification cryo-EM maps (**Fig. S2f,g**)[33,34].

124 ***In situ* Cryo-ET reveals a branched-filament ultrastructure in ASC/caspase-1 puncta**

125 Three-dimensional cryo-ET image reconstructions show a dense network of branched filaments
126 in areas identified by cryo-CLEM as containing ASC-mCerulean or caspase-1 labelled with
127 FAM-FLICA (**Figs. 1c-e, 2a, S2g**). Filaments in cells expressing ASC-mCerulean had additional
128 density at the filament periphery, and a less distinct outline compared to filaments in cells
129 expressing WT ASC (**Fig. 1d,e**). This suggests the additional density is primarily attributable to
130 mCerulean, which at 27 kDa is larger than ASC (22 kDa), although other components such as
131 caspase-1 (which was shown by light microscopy to localize to ASC specks), may also
132 contribute to this density. A green fluorescent protein tag was similarly found to decorate cryo-
133 ET reconstructions of amyloid-like poly-Gly-Ala aggregates with additional densities[35]. Since
134 mCerulean was fused to the C-terminus of ASC, the presence of mCerulean at the filament
135 periphery supports a model in which the filaments are formed at their core by the N-terminal
136 PYD of ASC, with the CARD located in between the PYD and mCerulean. Indeed, the cryo-EM
137 structure of purified recombinant ASC PYD filaments and the NMR structure of full-length ASC,

138 taken together, suggest that the PYD forms the filament core (9-nm in diameter), with the
139 flexibly-linked CARD increasing the filament diameter to 16-18 nm[23,24]. In our cryo-ET
140 reconstructions, filaments containing WT ASC had a diameter of 11-15 nm, which increased to
141 22-30 nm for filaments containing ASC-mCerulean (**Figs. 1d,e**). Notably, a continuous core of
142 density 8-10 nm in diameter (**Fig. 2a-c**) was visible within the ASC-mCerulean filaments (for
143 which the cryo-ET images were of higher quality). Although fluorescence from ASC-mCerulean
144 and FAM-FLICA-labelled capsase-1 colocalized in iBMDMs (**Fig. S1e**), the resolution of cryo-
145 CLEM was insufficient to determine whether any of the cryo-ET filament densities corresponded
146 to caspase-1 or other components. We note, however, that caspase-1 (30 kDa) and
147 procaspase-1 (45 kDa) are both larger than ASC and would therefore be expected to increase
148 filament diameter significantly, if present with the same stoichiometry as ASC.

149 Filament length measurements showed that WT filaments were on average slightly
150 shorter (191 $\pm$ 74 nm, n = 54) than ASC-mCerulean filaments (245 $\pm$ 116 nm, n = 402), with
151 similarly broad length distributions (**Fig. 1f,g**). This difference could potentially be due to the
152 higher levels of ASC protein expression in iBMDMs expressing ASC-mCerulean, which also
153 express endogenous WT ASC. Analysis of the branching angles showed that the angle
154 distributions of untagged and tagged filaments were slightly different, with larger branching
155 angles more common in mCerulean-tagged filaments, potentially due to steric constraints from
156 the tag (**Fig. 1h**). Our filament branching angle measurements are likely underestimated as any
157 filaments with their axis closely aligned with the Z-axis – which would result in a large (70-90˚)
158 branching angle – would not have been detected due to the missing-wedge effect (from sample-
159 tilt limitations). Taken together with previously published structural data from purified proteins,
160 our cryo-ET reconstructions suggest ASC filaments form the backbone of inflammasome-
161 induced puncta, but that the branching of these filaments results in a structural scaffold that can
162 recruit and concentrate downstream effector proteins.

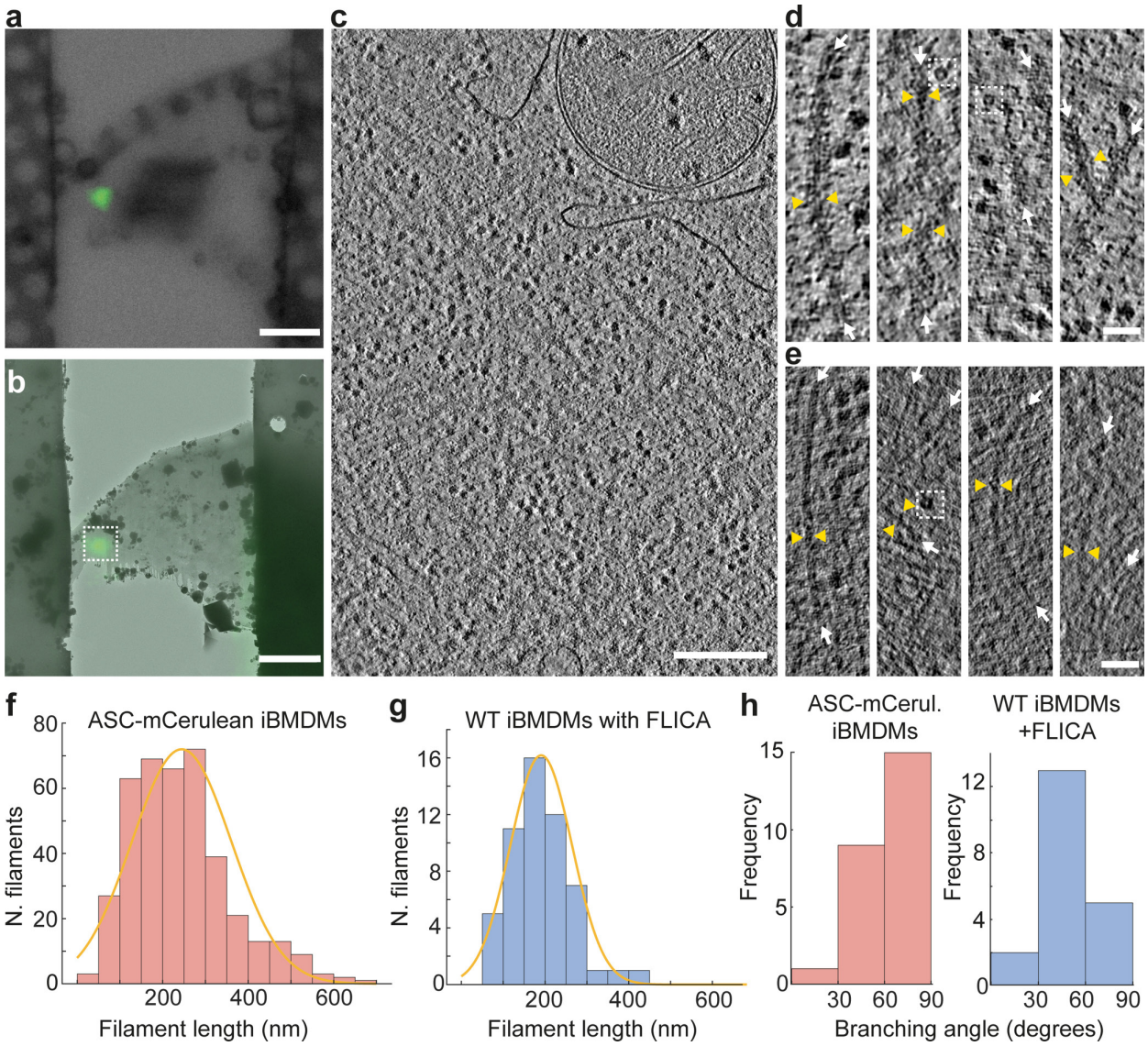

Figure 1. Cryo-ET image reconstructions of ASC-caspase 1 puncta in iBMDMs.

(a) Cryo-FM image of a lamella from an iBMDM expressing ASC-mCerulean. ASC-mCerulean fluorescence is shown (green), overlaid on a bright-field image. Scale bar, 5 µm.

(b) Cryo-FM image shown in (**a**) correlated and overlaid on a transmission cryo-EM map of the same lamella using the EC-CLEM ICY[36] plugin. Scale bar, 8 µm.

(c) Reconstructed cryo-ET volume (1.36-nm thick virtual tomographic slice), of the ASC-mCerulean punctum shown in (**a,b**). Scale bar, 250 nm.

(d-e) Galleries of filaments within ASC-mCerulean puncta, (**d**), or FAM-FLICA-labelled caspase-1 puncta, (**e**), in 4-nm thick virtual tomographic slices of iBMDMs. White arrows indicate

173 filament axes. Pairs of yellow triangles show filament thickness. Dashed white boxes
174 highlight ring-shaped densities. Scale bars, 50 nm.
175 **(f-g)** Filament length distribution in iBMDMs expressing ASC-mCerulean, (**f**), and in WT
176 iBMDMs labelled with FAM-FLICA, (**g**).
177 **(h)** Distribution of branching angles in ASC-mCerulean puncta (from 2 tomograms), and a
178 WT ASC punctum (1 tomogram).

179 For a more complete visualisation of the ASC speck ultrastructure in its cellular
180 environment, we generated a three-dimensional model of the filament network and other cellular
181 components including mitochondria, ER and ribosomes with IMOD[37]. This model showed that
182 puncta consist of several core regions of densely packed filaments separated by sparser
183 regions, with branching filaments connecting adjacent densely packed regions (**Fig. 2a, Movies**
184 **S3,S4**). Ribosomes were abundant within the filament network. Vesicles were also present, but
185 organelles including mitochondria were excluded.
186 We next investigated the equilibrium dynamics of ASC-mCerulean filaments by
187 fluorescence recovery after photobleaching (FRAP) in iBMDMs. We bleached circular regions
188 containing ASC-mCerulean puncta and imaged the ASC-mCerulean fluorescence intensity
189 before and after bleaching (**Fig. 2d**). Our data showed that ASC-mCerulean filament assemblies
190 have a small mobile fraction (6.9%; **Fig. 2e**). The dissociation rate (k_{off}) of ASC-mCerulean from
191 the imaged area was measured from the rate of fluorescence recovery as 0.023 ± 0.001 s^{-1}
192 (**Fig. 2d,e; Dataset S1**). Most of the observed fluorescence recovery was at the periphery of
193 puncta, suggesting that the ASC-mCerulean filaments inside the puncta are largely immobile
194 and are not in equilibrium with ASC monomers or oligomers in the cytosol (**Fig. 2d**).

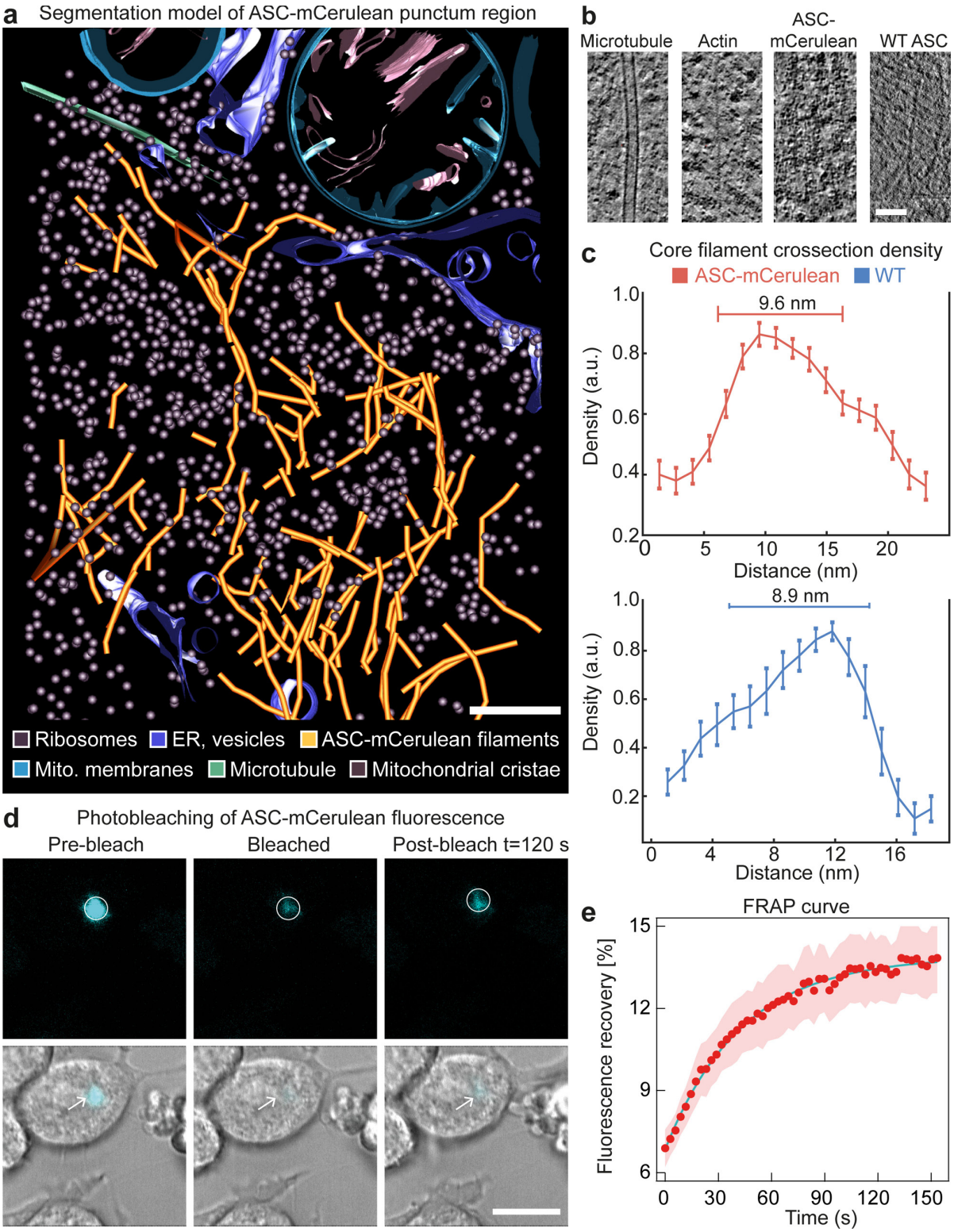

Figure 2. Visualization of the filament network and assembly dynamics of ASC puncta

(a) 3-D segmented model of the ASC-mCerulean punctum shown in **Fig. 1c**, generated with IMOD[37]. Scale bar, 250 nm.

199 **(b)** Representative instances of different filament types observed in 4-nm thick virtual
200 tomographic slices of iBMDMs. Scale bar, 50 nm.
201 **(c)** Average normalized density line profile of filament cross-sections, calculated from
202 projections of 16-nm thick virtual tomographic slices of iBMDMs. Error bars show standard
203 deviations (ASC-mCerulean, n = 25; WT, n = 13).
204 **(d)** Fluorescence recovery after photobleaching (FRAP) of ASC-mCerulean in iBMDMs. Scale
205 bar, 10 μm.
206 **(e)** FRAP curve used to calculate the ASC-mCerulean dissociation rate (k_{off}) from the bleached
207 area. Shaded area represents ± s.e.m. (n = 8). See **Dataset S1** for source data.

208 ***Trans*-Golgi-like vesicles are present within the ASC filament network**

209 How NLRP3 is activated by a broad range of different stimuli – including ion fluxes, reactive
210 oxygen species and mitochondrial damage – remains an open question. A common feature of
211 NLRP3 activation by these different stimuli is that the *trans*-Golgi network (TGN) is dispersed,
212 and NLRP3 locally accumulates at foci within the dispersed TGN[7,12]. These NLRP3 foci have
213 been proposed to serve as nucleation sites for ASC and caspase-1 recruitment and activation[7].
214 Consistent with previous studies, we observed dispersion of the TGN in WT iBMDM and THP-1
215 cells, and in iBMDMs expressing ASC-mCerulean (**Figs. 3a,b; S3a**). Moreover, NLRP3 partially
216 colocalized with the TGN marker TGN38 in WT iBMDMs primed with LPS, with or without
217 nigericin stimulation (**Fig. 3a**). In stimulated iBMDMs, ASC-mCerulean puncta were located
218 adjacent to anti-TGN38 fluorescence, but there was little direct overlap between the two
219 markers (**Fig. 3b**). In our tomographic reconstructions, vesicles with diameters of 50 to 300 nm
220 were observed within the ASC filament network (**Figs. 3c,d; S2g; S3b; Movies S3, S4**). We
221 observed similar vesicles within the filament network in chemically fixed ASC-mCerulean puncta
222 imaged by room temperature electron tomography (**Fig. S3c-e**). Notably, these vesicles had
223 low-density lumens, a feature characteristic of TGN vesicles[38]. Ribosomes were also found

224 embedded throughout the ASC filament network. Ring-shaped densities were occasionally
225 observed within tomograms of ASC puncta, but the resolution of the reconstructions was
226 insufficient to infer the composition of these features (**Fig. 1d**). Together, our cryo-ET and
227 fluorescence microscopy data supports the model that the dispersed TGN may serve as a
228 platform for ASC recruitment to multiple NLRP3 foci, which nucleate ASC polymerization, with
229 subsequent branching of ASC filaments driving growth into a micron-scale punctum.

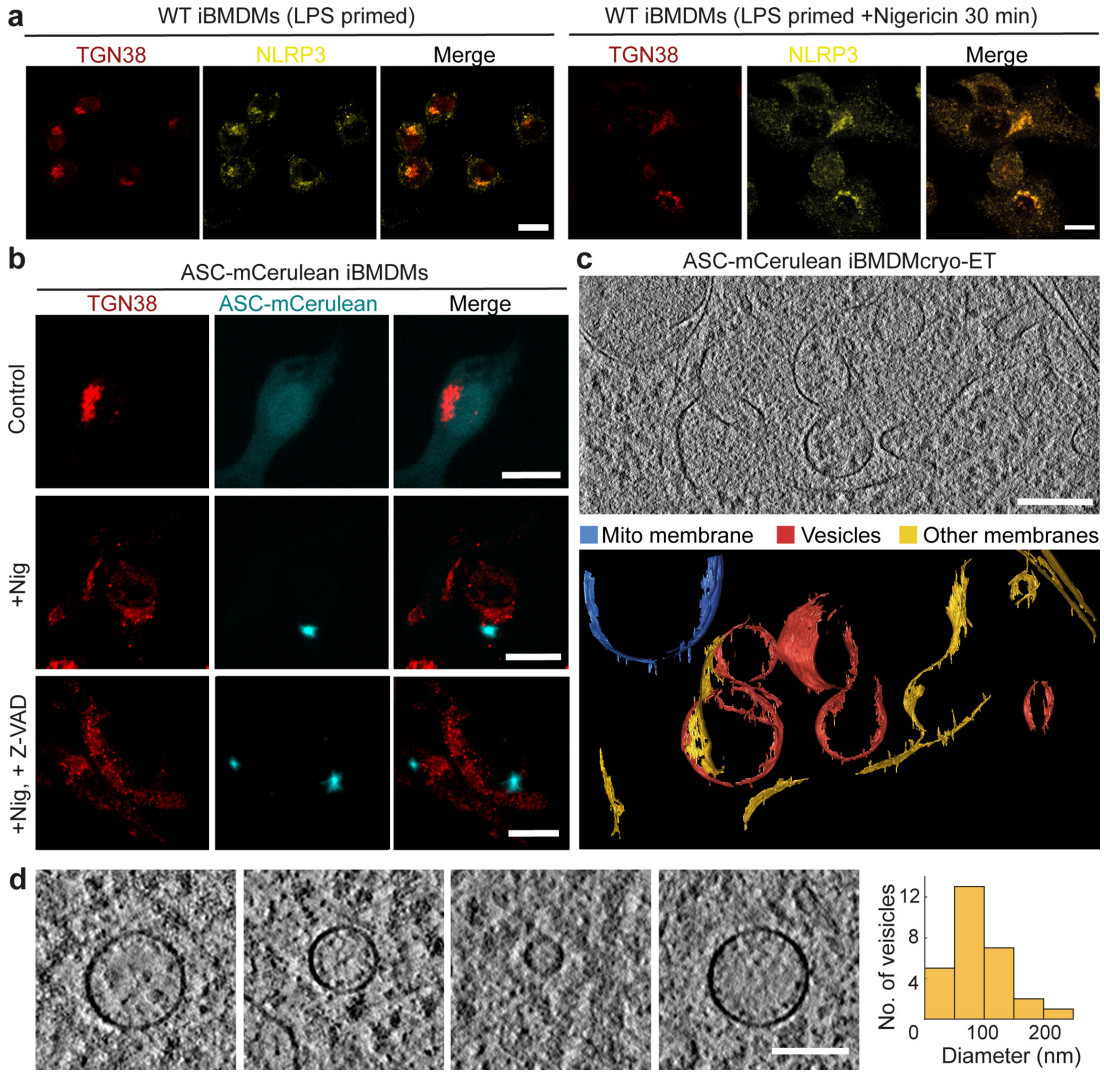

230

231 **Figure 3. TGN dispersion and TGN-like vesicles in ASC puncta after NLRP3 stimulation**

232 **(a)** Immunofluorescence microscopy of WT iBMDMs primed with LPS or stimulated with
233 nigericin. NLRP3 partially colocalized with TGN38. The TGN was dispersed following
234 stimulation. Scale bar, 10 μm.

235 **(b)** Immunofluorescence microscopy of iBMDMs expressing ASC-mCerulean before and after
236 stimulation with nigericin, or nigericin and caspase inhibitor Z-VAD-FMK. ASC-mCerulean
237 puncta were adjacent to anti-TGN38 fluorescence, but there was little overlap between the
238 two markers. Scale bar, 10 μm.
239 **(c)** 1.36-nm thick virtual tomographic slices of vesicles within the ASC-mCerulean filament
240 network in an iBMDM. Scale bar, 200 nm. Lower panel, 3-D segmentation model of the
241 same volume.
242 **(d)** Gallery of vesicles from tomographic reconstructions of cryo-FIB-milled ASC-mCerulean
243 iBMDMs. Scale bar, 100 nm. The histogram shows the vesicle diameter distribution.

244 Since NLRP3 inflammasome activation was reported to require transport of NLRP3 to
245 the MTOC[12,13], we examined the localization of ASC/caspase-1 puncta relative to the MTOC.
246 Fluorescent markers for ASC and caspase-1 did not colocalize with the MTOC components γ-
247 tubulin, pericentrin or ninein in WT or ASC-mCerulean iBMDMs stimulated with LPS and
248 nigericin (**Fig. S4a,b**). In stimulated THP-1 cells, ASC/caspase-1 puncta were on average closer
249 to the MTOC, with one quarter of puncta within 2 μm of the MTOC, but there was little direct
250 overlap between the fluorescent markers (**Fig. S4c**).

251 **Aberrant mitochondrial morphology during pyroptosis visualized by cryo-ET**

252 Mitochondria function as a nexus for multiple pathogen-sensing and damage-sensing signalling
253 pathways. Innate immune sensors of viral nucleic acids[39] and mitochondrial damage converge
254 on the outer mitochondrial membrane, and induce apoptosis or pyroptosis, depending on the
255 specific danger signal that is sensed[40,41]. We observed fragmentation of the filamentous network
256 of mitochondria in ASC-mCerulean iBMDMs following stimulation with LPS and nigericin, similar
257 to AIM-2 dependent mitochondrial remodelling[41], even prior to ASC punctum formation (**Fig.
258 4a).** Mitochondrial remodelling coincided with dissipation of the membrane potential (**Fig. 4b,
259 Fig. S5a**). To visualize and analyse the morphology of mitochondria soon after inflammasome

260 activation we performed cryo-ET reconstructions of mitochondria following LPS priming and
261 nigericin stimulation to induce ASC speck formation. In LPS primed iBMDMs expressing ASC-
262 mCerulean, a 30-min stimulation with nigericin resulted in mitochondria with a more rounded
263 overall shape and smaller size than in unstimulated cells (**Fig. 4c**). Cryo-ET reconstructions and
264 segmentation models of WT iBMDMs 1-h post-stimulation showed that the mitochondria in
265 these cells had an abnormal ultrastructure, with the inner membranes forming concentric tubular
266 structures instead of the regularly spaced lamellar cristae observed in unstimulated cells (**Fig.**
267 **4c,d**). To quantify the changes in mitochondrial morphology associated with ASC-dependent
268 signalling, four parameters were extracted and measured using Fiji[42]: cristae spacing, inner-to-
269 outer membrane spacing, cristae lumen width and cristae apex angles (**Fig. 5a,b**). We found the
270 cristae spacing to be two- to fourfold smaller in pyroptotic mitochondria than in healthy
271 mitochondria. The other three parameters were not significantly different.

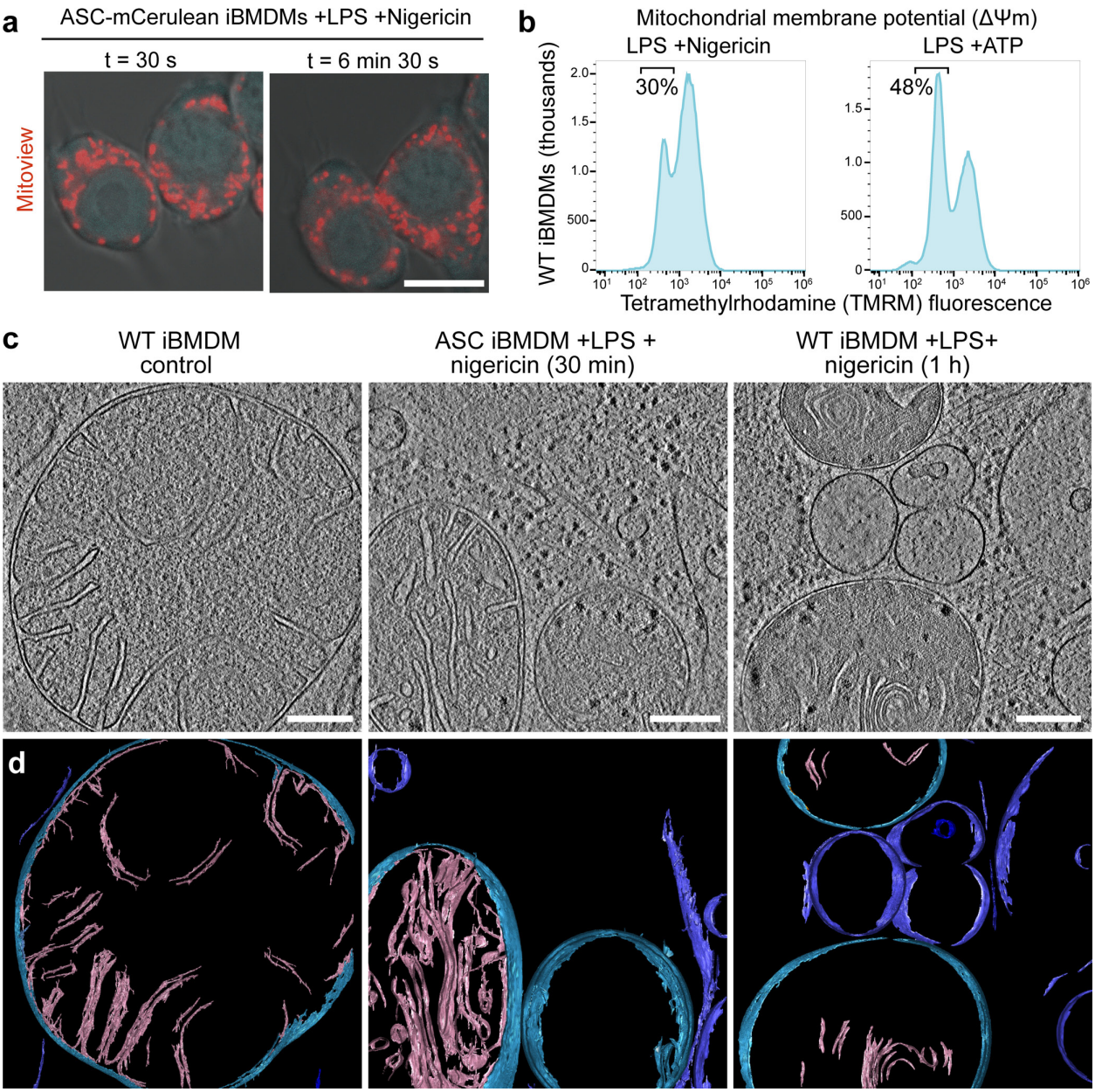

Figure 4. Remodelling of mitochondrial cristae after activation of NLRP3 inflammasome.

(a) Snapshots of live ASC-mCerulean iBMDMs labelled with a MitoView mitochondrial dye. Overlaid fluorescence and bright-field images show soon fragmentation of the mitochondrial network prior to ASC-speck formation. Scale bar 10 μm.

(b) Flow cytometry histogram of iBMDMs stained with tetramethylrhodamine (TMRM), a dye sensitive to mitochondrial membrane potential, ΔΨm. Cells were stimulated with LPS and nigericin (left), or LPS and ATP (right) for 30 min.

280 **(c)** Reconstructed cryo-ET tomographic slices of an unstimulated iBMDM (left); ASC-mCerulean
281 iBMDMs stimulated with LPS and nigericin for 30 min (centre); or WT iBMDMs, stimulated
282 with LPS and nigericin for 1 h (right).
283 **(d)** 3-D segmentation models of the outer and inner envelope membranes (purple) and cristae
284 membranes (pink) in the tomographic slices shown immediately above in (**c**).

285 **Discontinuities in the outer membranes of mitochondria during pyroptosis**

286 During apoptosis, the Bax and Bak proteins create large disruptions in the outer mitochondrial
287 membrane[40,43]. Our cryo-ET reconstructions showed that mitochondria in pyroptotic iBMDMs
288 stimulated with LPS/nigericin lacked any such large outer-membrane disruptions. We did,
289 however, identify small discontinuities in the outer mitochondrial membrane in some of the
290 stimulated ASC-mCerulean and WT iBMDMs (**Fig. 5c,d**). The size of these gaps varied from 10
291 to 22 nm (**Fig. S5b**). The presence of an intact inner membrane adjacent to the gap in the outer-
292 membrane implied that the gap was not due to the missing wedge effect or the anisotropic
293 resolution of cryo-ET tomograms[44].

294 The presence of 10-22-nm gaps in the outer membranes of mitochondria during
295 pyroptosis raises the question of whether these gaps cause mitochondrial outer membrane
296 permeabilization (MOMP) during inflammasome stimulation. To address this question, we
297 measured the cryo-EM density in the intermembrane space and in an adjacent cytosolic area,
298 where outer-membrane gaps were present. Unexpectedly, we found that the density at sites
299 where outer membrane gaps were present was higher than in the cytosol, indicating an increase
300 in macromolecular density at gap sites (**Fig. 5e,f**). In contrast, at sites where both membranes
301 were intact the intermembrane space had a lower density than the cytosol, as expected. The
302 increased cryo-ET density at gap sites spanned 10-22 nm along the Z-axis, matching the
303 dimensions of the gaps in X and Y. We conclude that protein-rich disruptions of the outer
304 mitochondrial membrane 10-22 nm in diameter form during pyroptosis.

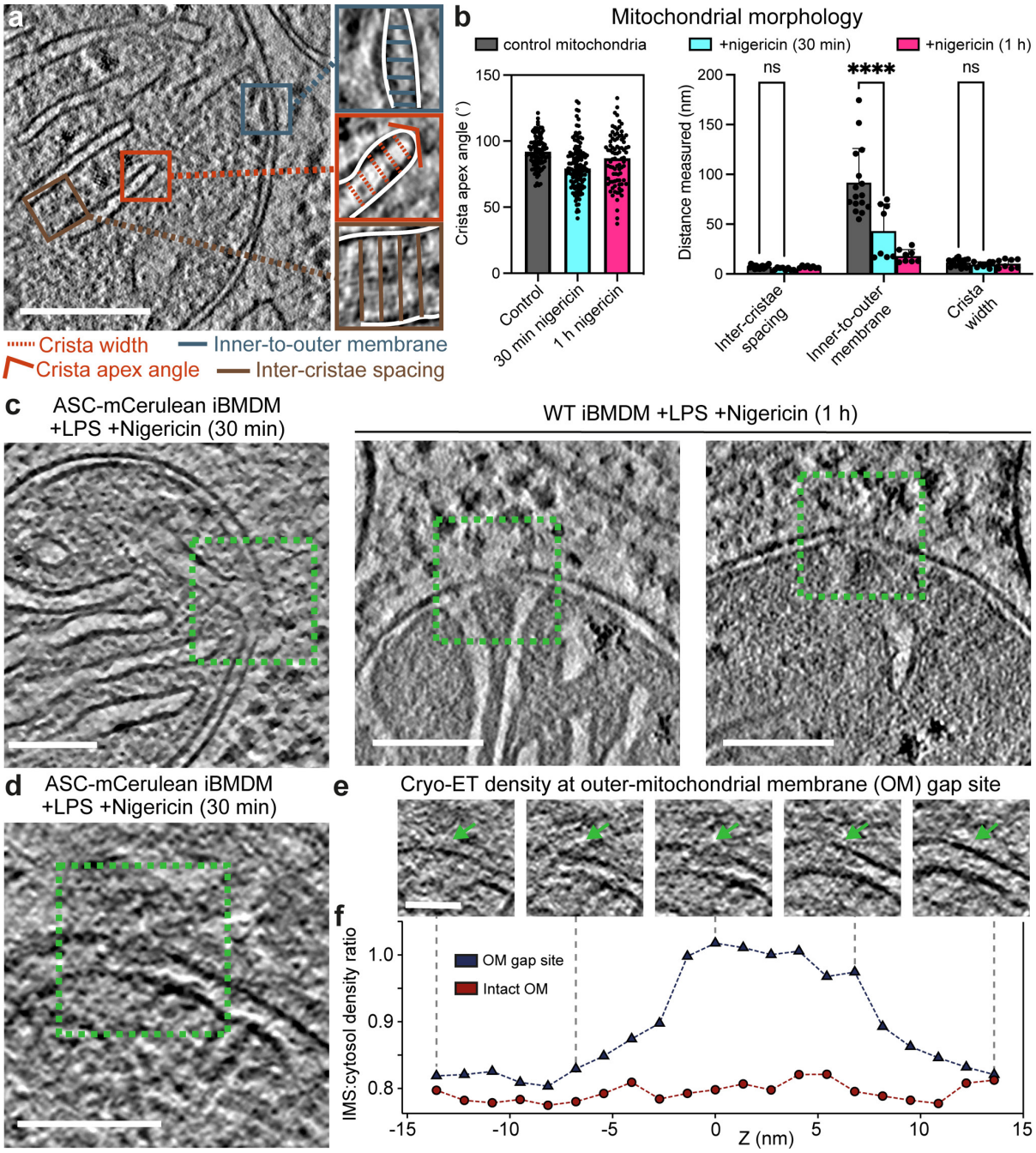

Figure 5. Outer mitochondrial membrane discontinuities in pyroptotic cells.

(a) Cryo-ET reconstruction of a mitochondrion in an unstimulated WT iBMDM with closeup panels defining the following morphological parameters: inner-to-outer membrane spacing, inter-cristae spacing, crista width and crista apex angle.

(b) Quantitative analysis of the morphological parameters quantified in (**a**) in 3-D segmented surfaces of the mitochondrial membranes, as shown in (**Fig. 4d**). Error bars represent

312 standard deviation between measurements. Parameters were measured from four
313 tomograms for the control and two tomograms for each of the nigericin-stimulated samples.
314 Error bars represent standard deviation from the mean. For the crista apex angles: “control”,
315 n = 327; “30 min”, n = 187; “1 h”, n = 96. For other parameters: “control”, n =16; “30 min”, n
316 = 8; “1 h”, n = 8. Statistical test: two-way ANOVA, ns, $P > 0.05$; ****, $P < 10^{-4}$. See **Dataset**
317 **S3** for source data.

318 **(c)** Cryo-ET reconstructions of mitochondria in ASC-mCerulean iBMDMs stimulated with
319 nigericin for 30 min (left) and in WT iBMDMs stimulated with nigericin for 1 h (centre, right).
320 Dashed boxes denote outer-membrane discontinuities. Scale bars, 100 nm.

321 **(d)** Higher magnification view of a mitochondrial outer-membrane discontinuity (dashed box).
322 Scale bar, 100 nm.

323 **(e)** Z-stack series for the boxed region in (**d**). Arrows mark the outer-membrane discontinuity.
324 Scale bar, 20 nm.

325 **(f)** Quantitative analysis of the cryo-ET density at the outer-membrane (OM) gap site in the Z-
326 stack series shown in (**e**), and at a site in the same tomogram with intact inner and outer
327 membranes. The graph plots the average pixel density ratio $\langle\rho(\mathrm{IMS})\rangle/\langle\rho(\mathrm{cyt})\rangle$ for each Z-
328 slice, where $\langle\rho(\mathrm{IMS})\rangle$ and $\langle\rho(\mathrm{cyt})\rangle$ are the average pixel densities of circular areas 35.4 nm
329 in diameter, in the mitochondrial intermembrane space (IMS) and an adjacent cytosolic
330 area, respectively. See **Dataset S2** for source data.

331 **Discussion**

332 NLRP3 inflammasome signalling assemblies have long been known from fluorescence
333 microscopy imaging to form puncta, or specks, containing ASC and caspase-1. Room
334 temperature electron tomography of ASC puncta in fixed zebrafish sections[26] and iBMDMs (**Fig.**
335 **S3d**) showed a dense filament network within the punctum, but the chemical fixation and
336 staining agents precluded further ultrastructure from being resolved. Our cryo-ET

337 reconstructions, obtained in unstained and fully hydrated conditions, show that the speck is
338 formed of a filamentous network consisting of hollow-tube branched filaments with the
339 dimensions predicted for ASC filaments, based on structural studies of purified ASC PYD
340 filaments and full-length monomeric ASC[23,24]. The identification of a filamentous network
341 containing mCerulean-labelled ASC positively identifies the protein as the principal filament-
342 forming component in the puncta. These data are supported by analysis of similar structures in
343 wild-type cells labelled with a fluorescent caspase 1 substrate. The filament structure of the
344 ASC with an mCerulean tag on the C-terminus supports the model whereby the PYD forms the
345 filament core, and the CARD decorates the filament. The extensive filament branching visible in
346 the reconstructions is thought to depend on CARD-CARD interactions because the CARD is
347 required for puncta formation, whereas the ASC PYD alone forms unbranched filaments that
348 lack the structural stability that is inherent to a branched network[17,18,23-26].

349 The density of ASC filaments varied in the cryo-ET reconstructions, with multiple core
350 regions of densely packed filaments separated by sparser regions. This suggests that the
351 higher-order structure of the punctum was likely seeded by multiple oligomeric assemblies,
352 rather than growing concentrically from a single nucleation site. In contrast with huntingtin and
353 other neurotoxic protein aggregates, which exclude other macromolecules based on cryo-ET
354 reconstructions[45], the structural organisation of the ASC filament network allows ribosomes and
355 small TGN-like vesicles to be retained in the puncta, or to permeate through them. Permeability
356 of the ASC network to macromolecules could be important for efficient recruitment and release
357 of effector, substrate and product molecules. Permeability to vesicles would allow active
358 transport of TGN vesicles carrying activated inflammasome seed-oligomers from sites of NLRP3
359 activation to the site of punctum formation, as recently proposed[12]. Moreover, the ribosomes
360 within the puncta could potentially contribute to the pyroptotic signalling programme, for
361 example by expressing proteins required for signalling, or by responding to danger signals.

362 Indeed, NLRP3 signalling can be activated by translational arrest through direct and indirect
363 mechanisms[46], including binding of fungal polysaccharides to ribosomes[47].

364 Our cryo-ET reconstructions, in addition to revealing the novel ultrastructure of ASC
365 within the cell, also allowed morphometric analysis of mitochondria in the inflammasome
366 activated cellular environment. The clearest differences between mitochondria in inflammasome
367 activated cells and unstimulated cells were a two to fourfold reduction in cristae spacing, and
368 the appearance of protein-rich discontinuities of 10-20 nm in diameter in the outer membrane,
369 which are distinct from BAK/BAX macropores. Permeabilization of both the plasma membrane
370 and outer mitochondrial membrane was reported previously in cells undergoing caspase-1-
371 dependent pyroptosis after inflammasome activation[41]. Pore formation in the plasma membrane
372 by the N-terminal domain of gasdermin D (GSDMD) after cleavage by caspase-1 is required for
373 inflammasome-dependent pyroptosis[48]. The outer-membrane discontinuities in the mitochondria
374 of inflammasome-activated cells had similar dimensions to GSDMD pores, which have an
375 average inner diameter of 22 nm[48] (or 13-34 nm based on atomic force microscopy[49]). Future
376 studies are warranted to test the hypothesis that the outer-membrane gaps observed by cryo-
377 ET may correspond to mitochondrial GSDMD pores.

378 The filament branching and packing density within ASC puncta provide structural
379 integrity while allowing downstream signalling molecules to diffuse freely and bind at high
380 density within the network. Although many structural details of the NLR inflammasome signalling
381 machinery remain unclear, this study demonstrates the potential for combined cryo-CLEM and
382 cryo-ET approaches to extract detailed, hypothesis-generating ultrastructural information for
383 fully assembled innate immune signalling complexes in their cellular context.

384 **Materials and Methods**

385 **Mammalian cell culture.** Wild-type immortalized primary bone-marrow derived macrophages
386 (WT iBMDMs) and ASC-mCerulean iBMDMs, kindly provided by Eicke Latz (Univ. Bonn), were
387 cultured in Dulbecco's modified Eagle Medium high glucose (DMEM; Gibco, Waltham, MA,
388 USA), supplemented with 10% v/v foetal bovine serum (FBS; Gibco). Human monocytic THP-1
389 cells (European Collection of Authenticated Cell Cultures) were grown in Roswell Park Memorial
390 Institute (RPMI) 1640 Medium (Gibco), supplemented with heat inactivated 10% v/v FBS, 10
391 mM HEPES pH 7.4, 1 mM Sodium Pyruvate and 0.05 beta-mercaptoethanol. Cells were
392 checked regularly for mycoplasma contamination by MycoAlert™ mycoplasma detection kit
393 (Lonza) and cells were free of mycoplasma contamination.

394 **Inflammasome stimulation.** For stimulation of WT iBMDMs and ASC-mCerulean iBMDMs,
395 cells were primed with 200 ng/ml LPS for 3 h in Opti-MEM® (Gibco) or DMEM supplemented
396 with 10% FBS before NLRP3 stimulus was used. The following stimulus were used: 10 μM
397 nigericin (Sigma or Invivogen) and 5 mM ATP (pH adjusted to 7.4, Sigma) for 30 min or 60 min
398 with pan-caspase inhibitor Z-VAD-FMK (Invivogen) or carboxyfluorescein-labelled inhibitor of
399 caspase-1 YVAD (FAM-FLICA, ImmunoChemistry Technologies) for *in situ* cryo-ET sample
400 preparation unless otherwise specified. For stimulation of THP-1 cells, priming and stimulation
401 were performed in RPMI Medium and conditions were listed above. To stain active caspase-1,
402 the supernatant was removed following inflammasome stimulation; replaced with DMEM
403 supplemented with heat-inactivated 10% v/v FBS containing 0.5x reconstituted FAM-FLICA
404 (ImmunoChemistry Technologies).

405 **Cytokine measurement and immunoblotting.** IL-1β secretion was measured by ELISA as
406 previously described[27]. Briefly, supernatants were collected after inflammasome activation and
407 BD BioSciences OptEIA was used to measure mouse IL-1β concentration in cell supernatant
408 according to the manufacturer's instructions.

409 The cells were lysed in cell lysis buffer (150 mM NaCl, 50 mM Tris-HCl pH 8, 1% Triton
410 X-100, 1 mM PMSF, 10 μg/mL leupeptin, 1 μg/mL aprotinin) on ice for 10 min before
411 centrifugation. Supernatant was collected and boiled in SDS sample loading buffer for 5 min.
412 Following separation by 4-20% gradient SDS-PAGE, the proteins were transferred to a PVDF
413 membrane. Membrane was blocked in 5% milk in PBS + 0.2% Tween-20. The primary antibody
414 was rabbit monoclonal anti-mouse GSDMD (Abcam, ab209845, RRID:AB_2783550). The
415 secondary antibody was goat anti rabbit IgG-HRP (Santa Cruz Biotechnology, sc-2004,
416 RRID:AB_631746).

417 **Immunofluorescence staining.** For immunofluorescence, cells were plated as monolayer on
418 μ-Slide 8-Well chamber (ibiTreat, Ibidi, 80826) or 12-well chamber (removable, Ibidi, 81201).
419 Cells were primed and stimulated as above, and then fixed with 4% paraformaldehyde for 5 to
420 10 min at room temperature. Cells were permeabilised and blocked in 0.1% Saponin (Sigma,
421 47036) supplemented with 20% FBS (Gibco) or 2% Bovine Serum Albumin (Sigma, A7030) in
422 PBS with primary antibody overnight. Washing was performed before cells were incubated with
423 secondary antibodies. The following primary antibodies were used: rabbit anti-ASC rabbit
424 polyclonal pAb AL177, 1:200 dilution (AdipoGen, AG-25B-0006, RRID:AB_2490440); rabbit
425 anti-ASC monoclonal ASC/TMS1(D2W8U), 1:800 dilution (Cell Signalling Technology, 67824,
426 RRID:AB_2799736); goat anti-NLRP3 polyclonal, 1:200 dilution (Abcam, ab4207,
427 RRID:AB_955792); goat anti-IL-1β polyclonal, 1:500 dilution (R&D Systems, AF-401-NA,
428 RRID:AB_416684); mouse anti-γ-Tubulin monoclonal, 1:400 dilution (Sigma-Aldrich, T6557,
429 RRID:AB_477584); rabbit anti-TGN38 polyclonal, 1:250 dilution (Novus Biologicals, NBP1-
430 03495, RRID:AB_1522533); rabbit anti-TOM20 FL-145 polyclonal, 1:80 dilution (Santa Cruz
431 Biotechnology, sc-11415, RRID:AB_2207533). The Alexa Fluor secondary antibodies (488, 555,
432 568 and 647) used were: 488-labelled donkey anti-goat IgG (H+L) (1:500, ThermoFisher,
433 A11055, RRID:AB_2534102); 555-labelled goat anti-rabbit IgG(H+L) (1:500, ThermoFisher,

434 A21428 RRID:AB_141784); 568-labelled goat anti-mouse IgG (H+L) (1:500, ThermoFisher,
435 A11004, RRID:AB_2534072); 647-labelled goat anti-rabbit IgG (H+L) (1:500, ThermoFisher,
436 A21244, RRID:AB_2535812). After incubation with secondary antibodies at room temperature
437 for 1 h, cells were washed three times with blocking buffer, one time with PBS and final wash
438 with water before mounting with ProLong Gold Antifade Mountant with DAPI (ThermoFisher).

439 **Confocal fluorescence imaging.** Single point-scanning confocal microscopy was carried out
440 on a Zeiss (Oberkochen, Germany) LSM 780 or LSM 710 microscope using a 40x/1.3 NA Fluar
441 or 63x/1.4 NA Plan-apochromat oil immersion objective lens. The microscope was equipped
442 with 405, 458, 488, 514, 561 and 633 nm laser lines. Multi point-scanning confocal microscopy
443 was carried out on Visitech (Sunderland, UK) iSIM mounted on a Nikon (Tokyo, Japan) Ti2
444 microscope stand using a 100x/1.49 NA SR Apo TIRF oil immersion objective lens or a 60x/1.2
445 NA Plan Apo VC water immersion objective lens. The iSIM was equipped with 405, 445, 488,
446 561 and 640 nm laser lines and Hamamatsu (Hamamatsu, Japan) ORCA-Flash4.0 V3 sCMOS
447 cameras. Filter ranges: green (500-545 nm), red (593-624 nm). Live-cell samples were heated
448 to 37˚C and supplemented with 5% CO_2 using a microscope incubation chamber.

449 **Live-cell imaging and Fluorescence Recovery after Photobleaching (FRAP)**. ASC-
450 mCerulean iBMDMs were primed and induced as previously described with the presence of
451 caspase-1 inhibitor (Z-VAD-FMK). Confocal FRAP was performed on a Zeiss LSM 710
452 microscope equipped with a 63x/1.4 NA Plan-apochromat oil immersion objective lens and a
453 458 nm laser line for excitation and bleaching. The sample environment was heated to 37˚C and
454 supplemented with 5% CO_2 using a microscope incubation chamber. ASC-mCerulean speck
455 was photobleached with 100% laser power. Images were acquired at 3 s intervals. Images were
456 collected at three pre-bleach timepoints and for 160 s post-bleaching. Movies were analysed in
457 ImageJ/Fiji[42] using a customised script (https://github.com/jboulanger/imagej-
458 macro/tree/main/FRAP_Measure). Briefly, measures were normalised to account for the general

459 photobleaching caused by image acquisition as well as sample motion over time. Normalised
460 fluorescence intensity measurements were obtained after background and bleaching
461 corrections. The timeframe varied for experiments (n = 8). Each measurement was interpolated
462 using the normalised fluorescence intensity measurements and imported to Python for plotting
463 of the fluorescence intensity curve.

464 **Quantification of Mitochondrial membrane potential.** After 30 min of inflammasome
465 stimulation as described above, iBMDMs were incubated with 20 nM TMRM (Life Technologies)
466 for 15 min. iBMDMs were incubated for 3 h in 50 μM of the mitochondrial uncoupler carbonyl
467 cyanide 3-chlorophenylhydrazone (CCCP; ThermoFisher, M20036). Control samples included:
468 untreated; TMRM+; TMRM+CCCP+; TMRM+LPS+ iBMDMs. TMRM fluorescence was
469 quantified by flow cytometry and data were acquired on Eclipse flow cytometer (Sony
470 Biotechnology). Quantification was set at 100,000 for cell count and a spectrum window of (FL3
471 (595BP)) was used to detect TMRM signal. Data were analysed and visualised using Flowjo10
472 (TreeStar, Ashland, Oregon, USA).

473 **Cryo-ET sample preparation.** Quantifoil finder grids (R2/1 or R2/2, Au 200 mesh grid,
474 Quantifoil Micro Tools, Germany) were glow discharged with a 30 mA current for 30 s using
475 Edwards Sputter Coater (S150B). Then grids were sterilized by UV irradiation for 10 min and
476 immersed in PBS supplemented with fibronectin solution (10 μg/ml, Sigma) overnight in 8-well
477 or coculture wells (ibidi). Grids were washed with PBS three times. Cells were seeded in 8-well
478 or coculture wells (ibidi) and incubated overnight at 37˚C and 5% CO_2. Cells cultivated on grids
479 were primed, induced with inflammasome stimuli and were plunge-frozen in liquid ethane using
480 Leica EM GP2 cryo-plunger. Prior to plunging, 4 μl of cell culture medium was added to the cell
481 side and backside blotting was applied for 6-8 s. The chamber conditions were maintained at
482 37˚C, 100% humidity during freezing. Grids were stored in liquid nitrogen.

483 **Cryo-fluorescent light microscopy (Cryo-FM) and cryo-focused ion-beam (FIB) milling.**
484 Grids were screened for cells with ASC/caspase-1 speck by light microscopy using a cryo-FM
485 microscope (Leica EM Cryo CLEM, Leica Microsystems), equipped with a cryo-stage, an
486 ORCA-Flash4.0 V2 sCMOS camera (Hamamatsu Photonics) and a 50x/0.9 NA HCX PL APO
487 cryo-objective lens. Montage acquisition of grids was performed with Leica LAS X software,
488 while recording the following channels: green (L5 filter, 50 ms), far red (Y5 filter, 20 ms), and
489 brightfield (50 ms). Z-stacks were recorded at 0.5 µm with step size 21 for each grid square to
490 determine the best focus for the montage. The montage was completed by stitching the best
491 focus image from the Z-stack with Leica LAS X.

492 Lamellae were prepared using a Scios Dual Beam FIB scanning electron microscope
493 (SEM; ThermoFisher) equipped with a Quorum cryo-stage (PP3010T). The milling protocol was
494 adapted from previously published method[29]. Grids were coated with organometallic platinum
495 using the gas injection system (GIS; ThermoFisher) operated at RT, for 8 s, at 12 mm working
496 distance and 25˚ stage tilt. A first rough milling was performed at 25˚ stage tilt with a 30 kV ion
497 beam voltage and 1 nA current until the lamella thickness reached 10 µm. The micro-expansion
498 joints were applied to improve lamella stability[32] using the milling parameters listed above. Then
499 stage was tilted to 20˚ for all subsequent milling steps. Rough milling steps were applied as
500 following with 30 kV ion beam voltage: a 5 µm lamella thickness was reached with current 0.5
501 nA; 3 µm lamella thickness was reached with a 0.3 nA current; and 1 µm lamella thickness was
502 obtained with a 0.1 nA current. Fine milling to a final lamella thickness of approximately 200 nm
503 was performed with ion beam settings of 30 kV and 50 pA or 10 pA, or 10 kV and 23 pA or 11
504 pA.

505 Grids were loaded to a Linkam cryo-stage (CMS196V), and lamellae were imaged on a
506 Zeiss microscope equipped with Axiocam 503 mono and Colibri 7-illumination module R(G/Y)
507 CBV-UV. Z-stacks of the lamellae were acquired to identify ASC/caspase-1 specks using a 200-

508 300 nm step size. A projected cryo-fluorescent image was used to correlate with an SEM image
509 using the EC-CLEM plugin from ICY[36]. Registration between the lamella map and SEM image
510 was achieved by transforming coordinates using edges or salient features of the lamella. The
511 maximum projection Z-stack was then saved for correlation with SerialEM[32,33].

512 **Tilt-series acquisition and tomogram reconstruction.** Grids with a fluorescent lamella were
513 transferred to a 300 kV Titan Krios electron microscope (ThermoFisher) equipped with an
514 energy filter (Gatan). Movies were acquired with a K2 or K3 direct electron detector with
515 SerialEM[33,34]. Cryo-FM/EM correlation was then used to locate an area of interest for tilt-series
516 acquisition. Briefly, a medium-magnification montage EM map (MMM) of the lamella was
517 generated and a fluorescence map (FM) was loaded into SerialEM. The maps were correlated
518 through recognition of geometric edges of the lamella. Transformation of coordinates yielded an
519 overlay map which provided guidance for tilt-series acquisition. Tilt-series were collected at a
520 nominal 32,000x or 29,000x magnification, resulting in pixel size 3.4 Å or 2.7 Å, over a tilt range
521 of -60˚ to +60˚ with 1˚, or 2˚ increments, a total dose of 140-240 electrons/A^2 and a nominal
522 defocus range of -4 to -8 μm. A dose-symmetric scheme was used[50]. A pre-processing script
523 was used from SubTOM (by Dustin Morado; https://github.com/DustinMorado/subTOM).
524 Frames were aligned using IMOD[37]. Reconstruction was performed by weighted back-
525 projection, and segmentation with IMOD. The MATLAB script deconv from Warp[51] was used for
526 visualisation. Filament tracing was performed manually with IMOD and UCSF Chimera[52].
527 Membrane segmentation was performed with TomoSegMemTV[53].

528 **Quantifications and statistical analysis.** Filament lengths were measured using IMOD[37] from
529 six tomograms of ASC-mCerulean iBMDMs and one tomogram of WT iBMDMs labelled with
530 FAM-FLICA. Histograms were plotted with MATLAB. Branching angles were measured with
531 Fiji[42] and exported to MATLAB for plotting. The filament diameter was determined in Fiji by
532 measuring density profiles of 20-nm lines perpendicular to the ASC filament (15 pixels in width,

533 ASC-mCerulean tomogram with13.6 Å/pixel and WT ASC tomogram with 10.78 Å/pixel). The
534 grey value profiles were normalized to their maximal individual value. Normalized grey profile
535 were aligned and exported to Python for plotting. Similarly, diameters of trans-Golgi-like vesicles
536 were measured in Fiji and exported to MATLAB for plotting.

537 Mitochondrial tomograms were loaded in Fiji[42] and ROI manager was used to measure
538 morphological parameters, which were compared using Two-way ANOVA and plotted with
539 GraphPad Prism. For the inner-to-outer membrane spacing, the distance between the nearest
540 edges of the inner and outer membranes was measured. The cristae width was measured
541 between the inner membranes of the cristae. The spacing between cristae were measured
542 using the perpendicular distance between the internal border of the neighbouring cristae. The
543 inner-to-outer membrane spacing, cristae width and inter-cristae spacing were measured
544 perpendicular to the membranes, evenly spaced for each tomogram, with thirty values per slice,
545 for four slices per tomogram, from eight tomograms. The cristae apex angles were measured for
546 every tip visible in ten slices per tomogram. Every value was plotted along with the average. If
547 the end of a crista was flat, then the measurement of the two angles on either side was
548 measured. Any measurement was only taken if the internal border of the membrane was clearly
549 distinguishable from the matrix. All measurements were evenly spaced through each slice, to
550 give a value representative of the whole slice, using all the mitochondria present in each image.
551 All measurements were taken using 8 different tomograms: four control, two 30-min nigericin-
552 treated, and two 60-min nigericin-treated mitochondria.

553 For measurement of the outer-mitochondrial membrane gap density, we calculated the
554 density ratio as follows. A total of 21 virtual slices were selected in a region containing a visible
555 outer-membrane gap. The average pixel grey value was calculated from circular areas 13.6 nm
556 in diameter: three cytosolic areas, three inter-membrane space areas and an outer-membrane
557 gap area. This was repeated for each of the 21 virtual slices. The ratio of average outer-

558 membrane gap site to cytosolic grey value, and the ratio of average inter-membrane space site
559 to cytosolic grey value were calculated for each virtual slice. The grey area ratio was then
560 plotted with Igor (WaveMetrics, Inc.) to show the change of protein density in Z direction.

561 **Data availability**

562 Representative electron tomograms were deposited in EMDB with codes EMDB with codes
563 EMD-13585, EMD-13586, EMD-135XX and EMD-135XX. Other data are available from the
564 corresponding authors upon request.

565 **Code availability**

566 SubTOM scripts and instructions are available from Github
567 [https://github.com/DustinMorado/subTOM]. The FRAP ImageJ macro is available on Github
568 [https://github.com/jboulanger/imagej-macro/tree/main/FRAP_Measure].

569

570 **References**

571 1 Xue, Y., Enosi Tuipulotu, D., Tan, W. H., Kay, C. & Man, S. M. Emerging Activators and
572 Regulators of Inflammasomes and Pyroptosis. *Trends Immunol* **40**, 1035-1052,
573 doi:10.1016/j.it.2019.09.005 (2019).

574 2 Karczewski, K. J. *et al.* The mutational constraint spectrum quantified from variation in
575 141,456 humans. *Nature* **581**, 434-443, doi:10.1038/s41586-020-2308-7 (2020).

576 3 Landrum, M. J. *et al.* ClinVar: improvements to accessing data. *Nucleic Acids Res* **48**,
577 D835-D844, doi:10.1093/nar/gkz972 (2020).

578 4 Gong, T., Liu, L., Jiang, W. & Zhou, R. DAMP-sensing receptors in sterile inflammation and
579 inflammatory diseases. *Nature Reviews Immunology* **20**, 95-112, doi:10.1038/s41577-019-
580 0215-7 (2020).

581 5 Heneka, M. T., McManus, R. M. & Latz, E. Inflammasome signalling in brain function and
582 neurodegenerative disease. *Nature Reviews Neuroscience* **19**, 610-621,
583 doi:10.1038/s41583-018-0055-7 (2018).
584 6 Swanson, K. V., Deng, M. & Ting, J. P. The NLRP3 inflammasome: molecular activation
585 and regulation to therapeutics. *Nat Rev Immunol* **19**, 477-489, doi:10.1038/s41577-019-
586 0165-0 (2019).
587 7 Chen, J. & Chen, Z. J. PtdIns4P on dispersed trans-Golgi network mediates NLRP3
588 inflammasome activation. *Nature* **564**, 71-76, doi:10.1038/s41586-018-0761-3 (2018).
589 8 Shen, C., Sharif, H., Xia, S. & Wu, H. Structural and mechanistic elucidation of
590 inflammasome signaling by cryo-EM. *Current Opinion in Structural Biology* **58**, 18-25,
591 doi:10.1016/j.sbi.2019.03.033 (2019).
592 9 Diebolder, C. A., Halff, E. F., Koster, A. J., Huizinga, E. G. & Koning, R. I. Cryoelectron
593 Tomography of the NAIP5/NLRC4 Inflammasome: Implications for NLR Activation.
594 *Structure* **23**, 2349-2357, doi:10.1016/j.str.2015.10.001 (2015).
595 10 Zhang, L. *et al.* Cryo-EM structure of the activated NAIP2-NLRC4 inflammasome reveals
596 nucleated polymerization. *Science* **350**, 404-409, doi:10.1126/science.aac5789 (2015).
597 11 Hu, Z. *et al.* Structural and biochemical basis for induced self-propagation of NLRC4.
598 *Science* **350**, 399-404, doi:10.1126/science.aac5489 (2015).
599 12 Magupalli, V. G. *et al.* HDAC6 mediates an aggresome-like mechanism for NLRP3 and
600 pyrin inflammasome activation. *Science* **369**, doi:10.1126/science.aas8995 (2020).
601 13 Li, X. *et al.* MARK4 regulates NLRP3 positioning and inflammasome activation through a
602 microtubule-dependent mechanism. *Nat Commun* **8**, 15986, doi:10.1038/ncomms15986
603 (2017).
604 14 Oroz, J., Barrera-Vilarmau, S., Alfonso, C., Rivas, G. & de Alba, E. ASC Pyrin Domain Self-
605 associates and Binds NLRP3 Protein Using Equivalent Binding Interfaces. *Journal of*
606 *Biological Chemistry* **291**, 19487-19501, doi:10.1074/jbc.M116.741082 (2016).

607 15 Stehlik, C. *et al.* Apoptosis-associated speck-like protein containing a caspase recruitment
608 domain is a regulator of procaspase-1 activation. *J Immunol* **171**, 6154-6163,
609 doi:10.4049/jimmunol.171.11.6154 (2003).
610 16 Proell, M., Gerlic, M., Mace, P. D., Reed, J. C. & Riedl, S. J. The CARD plays a critical role
611 in ASC foci formation and inflammasome signalling. *The Biochemical journal* **449**, 613-621,
612 doi:10.1042/BJ20121198 (2013).
613 17 Dick, M. S., Sborgi, L., Rühl, S., Hiller, S. & Broz, P. ASC filament formation serves as a
614 signal amplification mechanism for inflammasomes. *Nature Communications* **7**, 11929,
615 doi:10.1038/ncomms11929 (2016).
616 18 Sahillioglu, A. C., Sumbul, F., Ozoren, N. & Haliloglu, T. Structural and dynamics aspects of
617 ASC speck assembly. *Structure* **22**, 1722-1734, doi:10.1016/j.str.2014.09.011 (2014).
618 19 Matyszewski, M. *et al.* Cryo-EM structure of the NLRC4(CARD) filament provides insights
619 into how symmetric and asymmetric supramolecular structures drive inflammasome
620 assembly. *J Biol Chem* **293**, 20240-20248, doi:10.1074/jbc.RA118.006050 (2018).
621 20 Gong, Q. *et al.* Structural basis for distinct inflammasome complex assembly by human
622 NLRP1 and CARD8. *Nat Commun* **12**, 188, doi:10.1038/s41467-020-20319-5 (2021).
623 21 Li, Y. *et al.* Cryo-EM structures of ASC and NLRC4 CARD filaments reveal a unified
624 mechanism of nucleation and activation of caspase-1. *Proc Natl Acad Sci U S A* **115**,
625 10845-10852, doi:10.1073/pnas.1810524115 (2018).
626 22 Sborgi, L. *et al.* Structure and assembly of the mouse ASC inflammasome by combined
627 NMR spectroscopy and cryo-electron microscopy. *Proc Natl Acad Sci U S A* **112**, 13237-
628 13242, doi:10.1073/pnas.1507579112 (2015).
629 23 Lu, A. *et al.* Unified polymerization mechanism for the assembly of ASC-dependent
630 inflammasomes. *Cell* **156**, 1193-1206, doi:10.1016/j.cell.2014.02.008 (2014).

24 de Alba, E. Structure and interdomain dynamics of apoptosis-associated speck-like protein containing a CARD (ASC). *J Biol Chem* **284**, 32932-32941, doi:10.1074/jbc.M109.024273 (2009).

25 Nambayan, R. J. T., Sandin, S. I., Quint, D. A., Satyadi, D. M. & de Alba, E. The inflammasome adapter ASC assembles into filaments with integral participation of its two Death Domains, PYD and CARD. *J Biol Chem* **294**, 439-452, doi:10.1074/jbc.RA118.004407 (2019).

26 Kuri, P. *et al.* Dynamics of in vivo ASC speck formation. *J Cell Biol* **216**, 2891-2909, doi:10.1083/jcb.201703103 (2017).

27 Man, S. M. *et al.* Inflammasome activation causes dual recruitment of NLRC4 and NLRP3 to the same macromolecular complex. *Proc Natl Acad Sci U S A* **111**, 7403-7408, doi:10.1073/pnas.1402911111 (2014).

28 Rigort, A. *et al.* Focused ion beam micromachining of eukaryotic cells for cryoelectron tomography. *Proc Natl Acad Sci U S A* **109**, 4449-4454, doi:10.1073/pnas.1201333109 (2012).

29 Schaffer, M. *et al.* Cryo-focused Ion Beam Sample Preparation for Imaging Vitreous Cells by Cryo-electron Tomography. *Bio Protoc* **5**, doi:10.21769/bioprotoc.1575 (2015).

30 Stutz, A., Horvath, G. L., Monks, B. G. & Latz, E. ASC speck formation as a readout for inflammasome activation. *Methods Mol Biol* **1040**, 91-101, doi:10.1007/978-1-62703-523-1_8 (2013).

31 Smolewski, P. *et al.* Detection of caspases activation by fluorochrome-labeled inhibitors: Multiparameter analysis by laser scanning cytometry. *Cytometry* **44**, 73-82, doi:10.1002/1097-0320(20010501)44:1<73::aid-cyto1084>3.0.co;2-s (2001).

32 Wolff, G. *et al.* Mind the gap: Micro-expansion joints drastically decrease the bending of FIB-milled cryo-lamellae. *Journal of Structural Biology* **208**, 107389, doi:10.1016/j.jsb.2019.09.006 (2019).

657 33 Schellenberger, P. *et al.* High-precision correlative fluorescence and electron cryo
658 microscopy using two independent alignment markers. *Ultramicroscopy* **143**, 41-51,
659 doi:10.1016/j.ultramic.2013.10.011 (2014).
660 34 Mastronarde, D. N. Automated electron microscope tomography using robust prediction of
661 specimen movements. *J Struct Biol* **152**, 36-51, doi:10.1016/j.jsb.2005.07.007 (2005).
662 35 Guo, Q. *et al.* In Situ Structure of Neuronal C9orf72 Poly-GA Aggregates Reveals
663 Proteasome Recruitment. *Cell* **172**, 696-705 e612, doi:10.1016/j.cell.2017.12.030 (2018).
664 36 Paul-Gilloteaux, P. *et al.* eC-CLEM: flexible multidimensional registration software for
665 correlative microscopies. *Nat Methods* **14**, 102-103, doi:10.1038/nmeth.4170 (2017).
666 37 Kremer, J. R., Mastronarde, D. N. & McIntosh, J. R. Computer Visualization of Three-
667 Dimensional Image Data Using IMOD. *Journal of Structural Biology* **116**, 71-76,
668 doi:10.1006/jsbi.1996.0013 (1996).
669 38 Donohoe, B. S. *et al.* Cis-Golgi cisternal assembly and biosynthetic activation occur
670 sequentially in plants and algae. *Traffic* **14**, 551-567, doi:10.1111/tra.12052 (2013).
671 39 Hwang, M. S. *et al.* MAVS polymers smaller than 80 nm induce mitochondrial membrane
672 remodeling and interferon signaling. *The FEBS journal*, doi:10.1111/febs.14772 (2019).
673 40 Ader, N. R. *et al.* Molecular and topological reorganizations in mitochondrial architecture
674 interplay during Bax-mediated steps of apoptosis. *eLife* **8**, doi:10.7554/eLife.40712 (2019).
675 41 Yu, J. *et al.* Inflammasome activation leads to Caspase-1-dependent mitochondrial damage
676 and block of mitophagy. *Proc Natl Acad Sci U S A* **111**, 15514-15519,
677 doi:10.1073/pnas.1414859111 (2014).
678 42 Schindelin, J. *et al.* Fiji: an open-source platform for biological-image analysis. *Nat Methods*
679 **9**, 676-682, doi:10.1038/nmeth.2019 (2012).
680 43 McArthur, K. *et al.* BAK/BAX macropores facilitate mitochondrial herniation and mtDNA
681 efflux during apoptosis. *Science* **359**, doi:10.1126/science.aao6047 (2018).

682 44 Koning, R. I., Koster, A. J. & Sharp, T. H. Advances in cryo-electron tomography for biology
683 and medicine. *Ann Anat* **217**, 82-96, doi:10.1016/j.aanat.2018.02.004 (2018).
684 45 Bauerlein, F. J. B., Fernandez-Busnadiego, R. & Baumeister, W. Investigating the Structure
685 of Neurotoxic Protein Aggregates Inside Cells. *Trends Cell Biol* **30**, 951-966,
686 doi:10.1016/j.tcb.2020.08.007 (2020).
687 46 Vyleta, M. L., Wong, J. & Magun, B. E. Suppression of ribosomal function triggers innate
688 immune signaling through activation of the NLRP3 inflammasome. *PLoS One* **7**, e36044,
689 doi:10.1371/journal.pone.0036044 (2012).
690 47 Briard, B. *et al.* Galactosaminogalactan activates the inflammasome to provide host
691 protection. *Nature* **588**, 688-692, doi:10.1038/s41586-020-2996-z (2020).
692 48 Xia, S. *et al.* Gasdermin D pore structure reveals preferential release of mature interleukin-
693 1. *Nature*, doi:10.1038/s41586-021-03478-3 (2021).
694 49 Mulvihill, E. *et al.* Mechanism of membrane pore formation by human gasdermin-D. *EMBO*
695 *J* **37**, doi:10.15252/embj.201798321 (2018).
696 50 Hagen, W. J. H., Wan, W. & Briggs, J. A. G. Implementation of a cryo-electron tomography
697 tilt-scheme optimized for high resolution subtomogram averaging. *J Struct Biol* **197**, 191-
698 198, doi:10.1016/j.jsb.2016.06.007 (2017).
699 51 Tegunov, D. & Cramer, P. Real-time cryo-electron microscopy data preprocessing with
700 Warp. *Nat Methods* **16**, 1146-1152, doi:10.1038/s41592-019-0580-y (2019).
701 52 Pettersen, E. F. *et al.* UCSF Chimera--a visualization system for exploratory research and
702 analysis. *J Comput Chem* **25**, 1605-1612 (2004).
703 53 Martinez-Sanchez, A., Garcia, I., Asano, S., Lucic, V. & Fernandez, J. J. Robust membrane
704 detection based on tensor voting for electron tomography. *J Struct Biol* **186**, 49-61,
705 doi:10.1016/j.jsb.2014.02.015 (2014).

706 54 Ader, N. R. & Kukulski, W. triCLEM: combining high-precision, room temperature CLEM
707 with cryo-fluorescence microscopy to identify very rare events. *Method Cell Biol* **140**, 303-
708 320, doi:10.1016/bs.mcb.2017.03.009 (2017).
709 55 Kukulski, W. *et al.* Correlated fluorescence and 3D electron microscopy with high sensitivity
710 and spatial precision. *Journal of Cell Biology* **192**, 111-119, doi:10.1083/jcb.201009037
711 (2011).
712

713 **Acknowledgements**

714 We acknowledge the MRC Laboratory of Molecular Biology (LMB) Electron Microscopy (EM)
715 Facility for access and support in EM sample preparation and data collection, and the Flow
716 Cytometry Facility for access and training. We are grateful to Dustin Morado for assisting in
717 cryo-ET data collection and image processing. We acknowledge the MRC LMB Light
718 Microscopy Facility, in particular Jonathan Howe, for access and support imaging data
719 collection. We are grateful for access to the MRC-LMB Scientific Computing facilities. We thank
720 Kendra E. Leigh, Wanda Kukulski, Emma Jones, Robert Pickering, Maria Daly, Victoria L. Hale
721 and Zunlong Ke for helpful advice and discussions. This work was supported by Wellcome
722 Senior Research Fellowship 217191/Z/19/Z to Y.M.; a PhD studentship to Y.L. from the China
723 Scholarship Council and Cambridge Trust; and Wellcome Investigator Award 108045/Z/15/Z to
724 C.E.B.

725 **Author contributions**

726 Y.L., L.J.H., C.E.B and Y.M. conceived the experiments. Y.L., H.Z. and J.H. collected light
727 microscopy data. Y.L. and J.B. analysed light microscopy data. Y.L., A.C.B. and C.H. prepared
728 cryo-EM samples, performed CLEM imaging and collected cryo-ET data. Y.L. processed the
729 cryo-ET data. Y.L. and H.A. analysed the cryo-ET data and flow-cytometry analysis. Y.L. and

730 L.J.H. performed cell-based assays. Y.L, C.E.B and Y.M. wrote the manuscript with input from
731 all authors. Project supervision, administration and funding acquisition, C.E.B. and Y.M.

732 **Competing interests**

733 C.E.B are Y.M. are consultants for Related Sciences LLC and have profits interests in Danger
734 Bio LLC. CEB is on the SAB of NodThera and Lightcast.

735

736

Cryo-electron tomography of ASC sites in pyroptotic cells

Liu *et al.*

Supplementary Information

Supplementary Materials and Methods

Figures S1-S5

749 **Supplementary Materials and Methods**

750 **Correlative fluorescence microscopy and electron tomography of resin-embedded cells.**
751 Correlative fluorescence microscopy and electron tomography (RT-CLEM) of resin-embedded
752 cells was performed as described[40,54]. Briefly, ASC-mCerulean cells were grown on carbon-
753 coated 3 mm sapphire discs (Wohlwend GmbH) in two-well chambers (ibidi) for 24 h before
754 priming and NLRPC-driven inflammasome stimulation as described above. Cells were stained
755 with MitoView far-red and FLICA before high pressure freezing with an HPM100 high pressure
756 freezing system (Leica Microsystems). Grids were imaged with a cryo-fluorescence microscope
757 (Leica EM Cryo CLEM, Leica Microsystems) to localise cells containing ASC-mCerulean
758 specks. Freeze substitution was preformed using 0.008% uranyl acetate in acetone and
759 embedded in Lowicryl HM20 (Polysciences) using an AFS2 (Leica Microsystems). Blocks were
760 sectioned into 300 nm thin sections using a microtome (Leica Microsystems) equipped with a
761 diamond knife (Diatome). The sections were collected on 200 mesh/300 mesh copper grids with
762 carbon support (Agar Scientific Ltd). TetraSpeck 100-nm microspheres were diluted 1:100 in
763 PBS and applied to the sections for use as fiducial markers for correlation. Sections were
764 imaged on a Nikon Ti2 wide field microscope equipped with a Niji LED light source (Bluebox
765 Optics, Blackwood, UK), a x100/1.49 NA Apo TIRF oil immersion objective lens and a Neo
766 sCMOS DC-152Q-C00-FI camera (Andor Technology, Belfast, UK). Filters: mCerulean (89006
767 filter set, Chroma Technology, Bellows Falls, USA), fluorescein (49002 filter set, Chroma),
768 MitoView Far Red (49006 filter set, Chroma). EM images were collected using a Tecnai F20
769 electron microscope (ThermoFisher) operated at 200 kV and a high-tilt tomography holder
770 (Fischione Instruments; Model 2020). An image montage of regions of interest was acquired on
771 a BM-Orius detector using TEM mode at 150-200 µm defocus using SerialEM v3.8.0[34] at a pixel
772 size of 1.1 nm. The correlation between the montaged map and fluorescent map was performed
773 by image transformation of registered fiducial markers in both image modalities as previously

774 described[55]. Tilt-series were acquired from approximately -60 to +60 with 1˚ increment at a pixel

775 size of 1.1 nm. Samples were rotated 90˚ to acquire dual axis tilt-series. Tomograms were

776 reconstructed and visualised with IMOD[37].

777
778
779
780

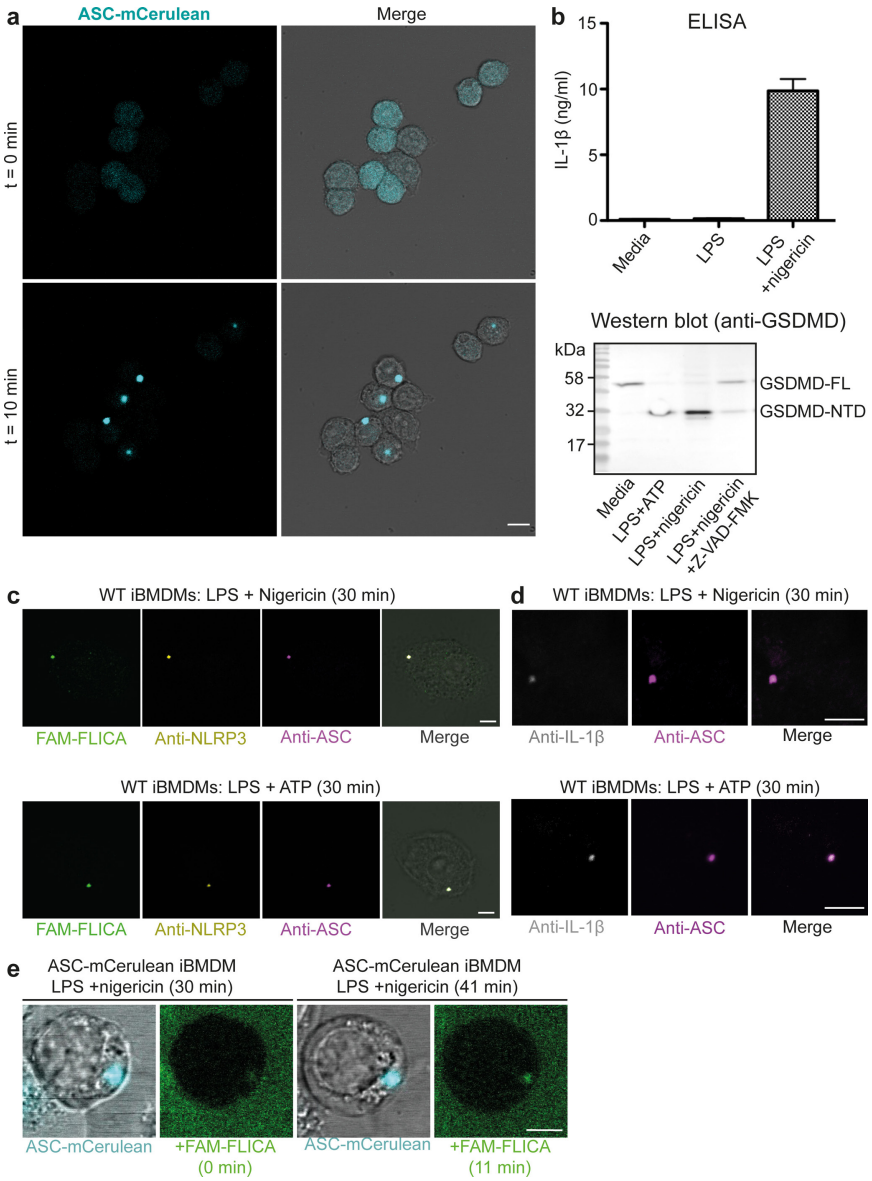

Figure S1. Tracking NLRP3 inflammasome activation in iBMDMs with fluorescence microscopy and biochemical assays.

(a) Snapshots of live iBMDMs expressing ASC-mCerulean. ASC specks formed within 10 min of NLRP3 inflammasome activation with LPS and nigericin. Merge, overlay of fluorescence and bright-field images. Scale bar, 10 μm.

(b) Biochemical assays of inflammasome activation in ASC-mCerulean iBMDMs: upper panel, ELISA measuring IL-1β secretion; lower panel, Western blot showing proteolytic cleavage of GSDMD following different stimuli. FL, full-length. NTD, N-terminal domain.

(c) Fluorescence microscopy of WT iBMDMs stimulated with LPS and either nigericin or ATP. Caspase-1 was detected with FAM-FLICA. NLRP3 and ASC were detected by immunostaining. Scale bars, 5 μm.

(d) Immunofluorescence microscopy of WT iBMDMs stimulated with LPS and either nigericin or ATP, with staining for IL-1β and ASC. Scale bars, 5 μm.

(e) Snapshots of live ASC-mCerulean iBMDMs stained with FAM-FLICA after nigericin stimulation showing ASC-mCerulean colocalization with caspase-1 and FAM-FLICA fluorescence intensity increasing over time. Scale bar, 5 μm.

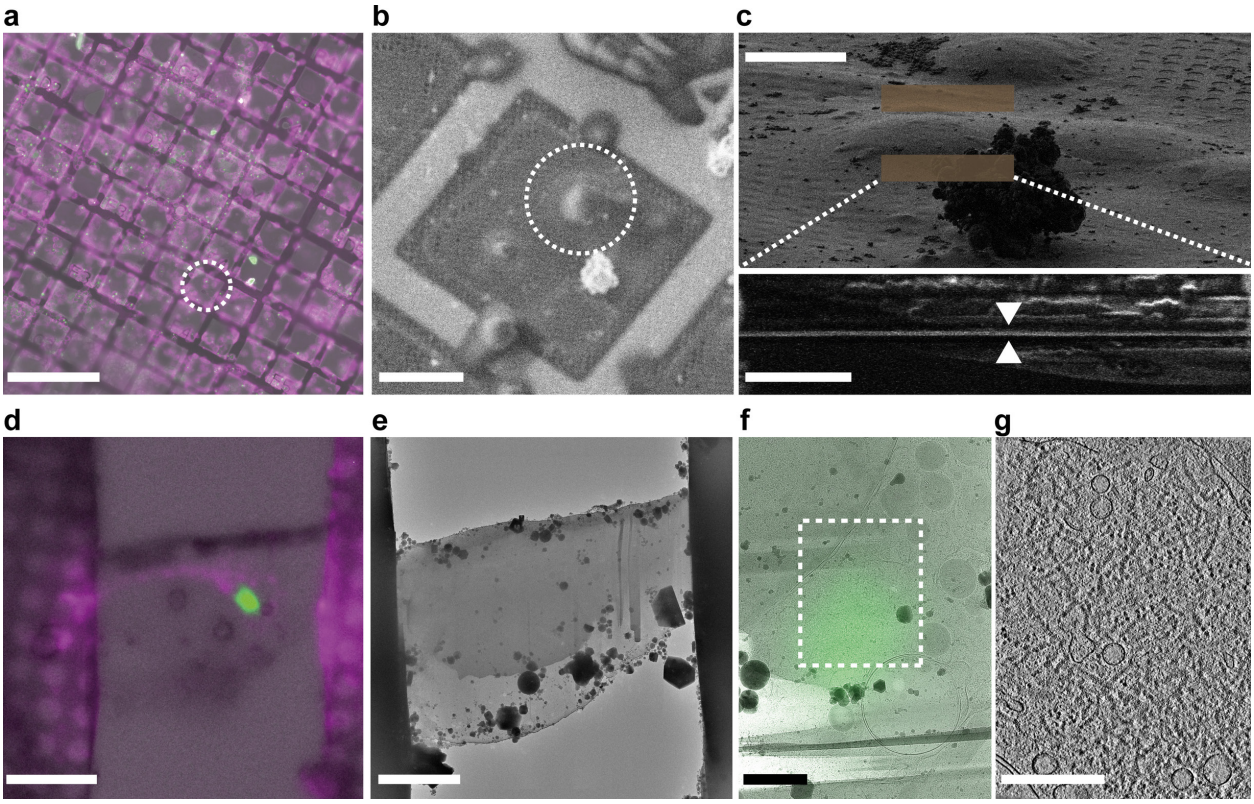

Figure S2. Workflow for correlative cryo-light and electron microscopy (cryo-CLEM).
(a) Cryo-fluorescence microscopy (cryo-FM) of ASC-mCerulean iBMDMs, with brightfield image overlaid. Cells were cultured on finder grids, primed with LPS, stimulated with nigericin for 30 min, labelled with MitoView and FAM-FLICA, vitrified, and then imaged. The white circle denotes one area of interest. Scale bar: 300 µm.
(b) Grids were transferred to a scanning electron microscope (SEM) fitted with a focused-ion-beam (FIB). The cell containing the area of interest, identified using the finder-grid markers, was imaged by SEM. Scale bar, 40 µm.
(c) SEM images of the area of interest before and after FIB milling: Upper panel, before FIB milling with initial target milling windows shown in brown (scale bar, 10 µm); lower panel, side-on view of the lamella after FIB milling (scale bar, 4 µm).
(d) Cryo-FM image of a lamella containing an ASC speck with brightfield image overlaid. Scale bar, 10 µm.
(e) Low magnification transmission cryo-EM map of the lamella shown in (**d**). Scale bar, 7 µm.
(f) Medium magnification cryo-EM map overlaid with the cryo-FM map after registration and transformation. The region of interest for tilt-series acquisition is boxed. Scale bar, 1 µm.
(g) Reconstructed tomographic slice acquired in the area marked in (**f**) containing the fluorescent signal. Several short filaments and small trans-Golgi-like vesicles were visible. Scale bar, 300 nm. See **Movie S4** for a tomogram of this region.

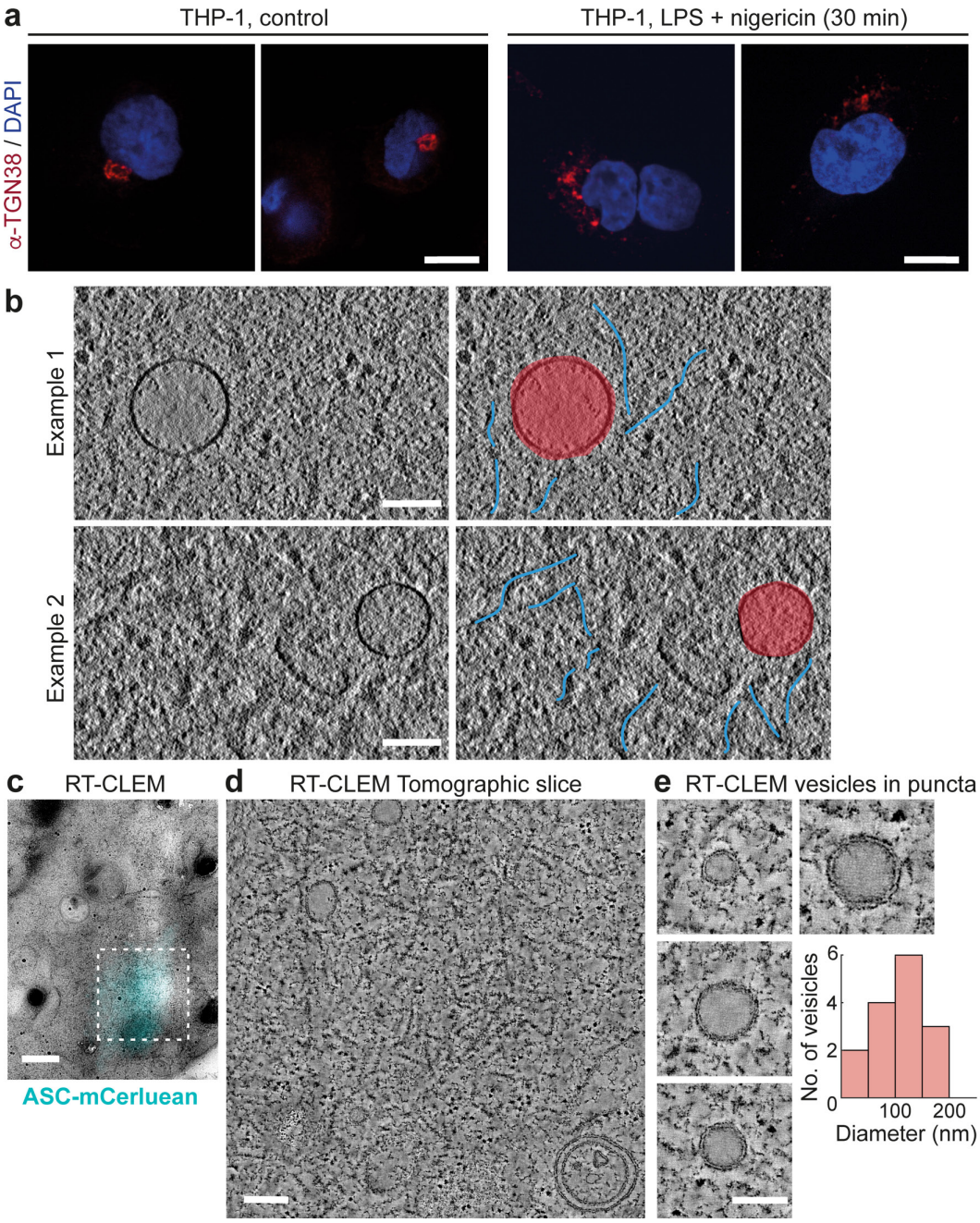

Figure S3. Imaging of *trans*-Golgi-like vesicles within ASC puncta.
(a) Fluorescence micrographs of THP-1 cells with and without stimulation with LPS and nigericin, with TGN (anti-TGN38) immunostaining. Scale bar, 10 µm.
(b) Two tomographic slices of ASC-mCerulean speck showing vesicles adjacent to filaments. Scale bars, 100 nm.
(c-e) CLEM of ASC-mCerulean iBMDMs stimulated with nigericin for 30 min, high-pressure frozen, chemically fixed, sectioned and imaged at room temperature (see Supplementary Materials and Methods). (**c**) Low magnification EM map overlaid with ASC-mCerulean fluorescence. Scale bar, 1 µm. (**d**) 5.5 nm-thick tomographic slice of in the region boxed in (c). Scale bar, 200 nm. (**e**) Tomographic slices showing vesicles with low-density lumens within ASC-mCerulean puncta. Scale bar, 100 nm. The histogram shows the vesicle diameter distribution.

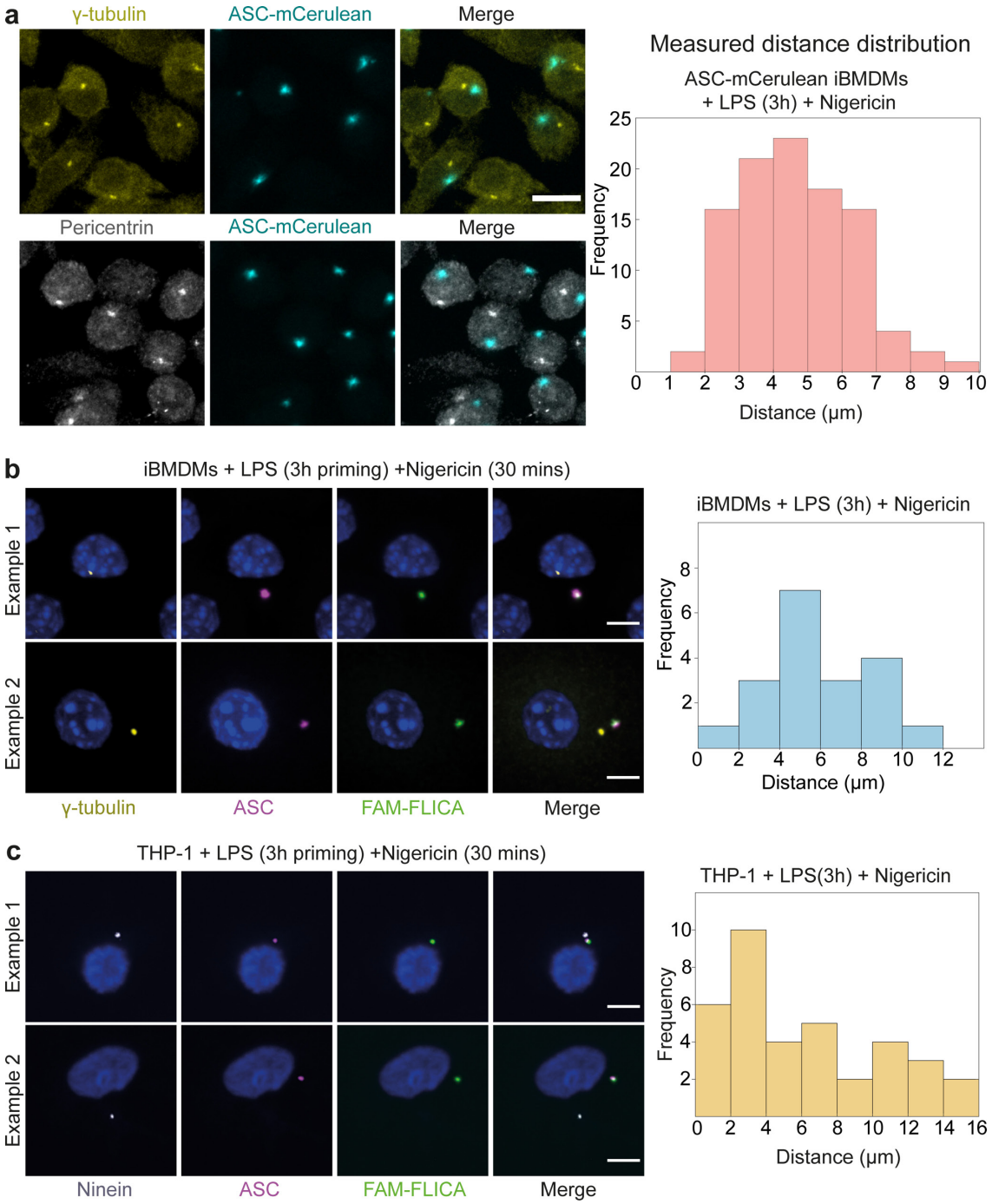

Figure S4. Localization of ASC and caspase-1 relative to MTOC-associated components.
(a) Fluorescence micrographs of ASC-mCerulean iBMDMs stimulated with LPS and nigericin, with γ-tubulin immunostaining. Scale bar, 10 μm. Right, distribution of the distance between ASC-mCerulean and anti-γ-tubulin fluorescence.
(b) Fluorescence micrographs of WT iBMDMs stimulated with LPS and nigericin. Cells were stained with FAM-FLICA, and with antibodies against γ-tubulin and ASC. Scale bar, 10 μm. Right, distribution of the distance between ASC/FAM-FLICA and anti-γ-tubulin fluorescence.
(c) Fluorescence micrographs of THP-1 cells stimulated with LPS and nigericin. Cells were stained with FAM-FLICA, and with antibodies against ninein and ASC. Scale bar, 10 μm. Right, distribution of the distance between ASC/FAM-FLICA and anti-ninein fluorescence.

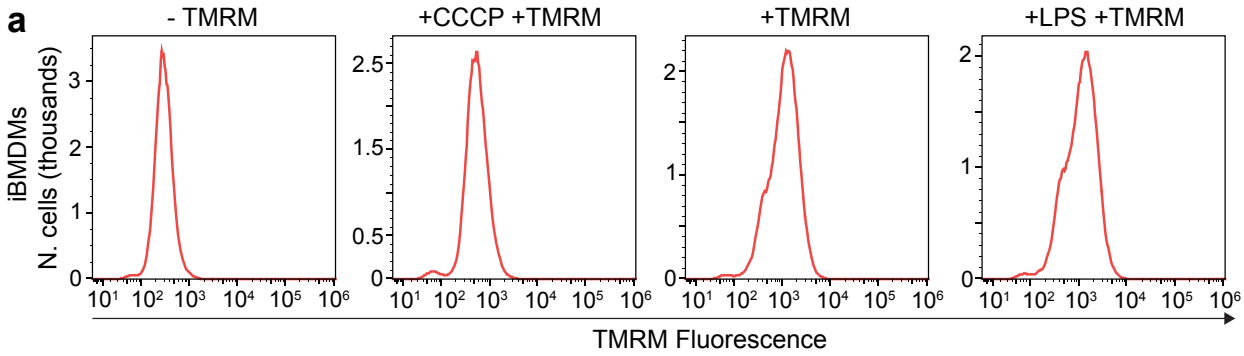

b

iBMDM type	Nigericin stimulation (min)	Gap width (nm)	Estimated gap depth (nm)
ASC-mCerulean	30	11	11
ASC-mCerulean	30	15	12
ASC-mCerulean	30	18	14
ASC-mCerulean	30	11	14
WT	60	20	-
WT	60	17	17

Figure S5. Functional and ultrastructural analyses of mitochondria in iBMDMs stimulated with nigericin.

(a) Additional flow cytometry histograms of iBMDMs. The following controls are shown to accompany **Fig. 4b**: cells with no TMRM staining; cells stained with TMRM and a potent mitochondrial uncoupling chemical, carbonyl cyanide 3- chlorophenylhydrazone (CCCP); cells stained with TMRM only; and cells primed with LPS and stained with TMRM.

(b) Measured sizes of outer-membrane discontinuities in cryo-ET reconstructions of mitochondria in WT and ASC-mCerulean iBMDMs, as partly shown in **Fig. 5c-e**.